Eruption dynamics of the 22-23 April 2015 Calbuco volcano (Southern Chile): analyses of tephra fall deposits

J. E. Romero [a], D. Morgavi [b], F. Arzilli [c], R. Daga [d,e], A. Caselli [e,f], F. Reckziegel [e,g], J. Viramonte [e,g], J. Díaz-Alvarado [a], M. Polacci [c], M. Burton [c], D. Perugini [b]

[a] Departamento de Geología, Universidad de Atacama. Av. Copayapu 485, Copiapó, Chile.

[b] Department of Physics and Geology, University of Perugia, Piazza dell'Università 06123 Perugia, Italy

[c] School of Earth, Atmospheric and Environmental Sciences, University of Manchester, M13 9PL Oxford Road, Manchester, United Kingdom.

[d] Laboratorio de Análisis por Activación Neutrónica, Centro Atómico de Bariloche, CNEA, Av. Bustillo km 9.5, 8400 Bariloche, Argentina.

[e] Consejo Nacional de Investigaciones Científicas y Técnicas (CONICET), Argentina.

[f] Laboratorio de Estudio y Seguimiento de Volcanes Activos (*LESVA*), Universidad Nacional de Río Negro, Roca 1242, (8332) Roca, Argentina.

[g] INENCO/GEONORTE Univ. Nacional de Salta-CONICET, Av. Bolivia 5150–4400, Salta, Argentina

Corresponding author**:** Jorge E. Romero

e-mail: jorge.romerom@alumnos.uda.cl

Tel.: +56 9 5418 2930

Abstract

After 54 years since its last major eruption in 1961, Calbuco volcano (Ensenada, Southern Chile) reawakened with few hours of warning on 22 April 2015 at 18:05 local time. The main explosive eruption consisted of two eruption pulses (lasting ~1.5 and 6 hours each one) on 22 and 23 April, producing stratospheric (>15 km height) eruption columns. The erupted materials correspond to porphyritic basaltic andesite (~55 wt. % of SiO_2). The tephra fall affected mainly the area northeast of the volcano and the finest ash was deposited over Southern Chile and Patagonia Argentina. We studied the tephra fall deposits of both pulses in terms of stratigraphy, distribution, volume, emplacement dynamics and eruption source parameters. Here, we show field observations that have been made 5-470 km downwind and distinguish five layers (Layers A, B, B1, C and D) representing different stages of the eruption evolution: eruption onset (Layer A; pulse 1), followed by the first paroxysmal event (Layer B; pulse 1), in some places interbedded by layer B1, tentatively representing the sedimentation of a secondary plume during the end of pulse 1. We recognized a second paroxysm (Layer C; pulse 2) followed by the waning of the eruption (Layer D; pulse 2). The total calculated bulk tephra fall deposit volume is 0.27±0.007 km^3 (0.11-0.13 km^3 dense rock equivalent), 38% of which was erupted during the first phase and 62% during the second pulse. This eruption was a magnitude 4.45 event (VEI 4 eruption) of Subplinian type.

Key words: Calbuco volcano, eruption chronology, tephra stratigraphy, Subplinian eruption.

1. Introduction

Calbuco (41°20'S-72°37'W, 2003 m a.s.l.) is an active and hazardous stratovolcano in the southern Andes of Chile (Stern et al., 2007), near the city of Ensenada and Puerto Montt (Southern Chile) (Fig. 1A, B). Almost 20 pyroclastic density current (PDCs) and 10 pumice fallouts have been generated by this volcano (Moreno & Naranjo, 2004; Watt et al., 2011) since postglacial times (<14 ky). Among 13 recognized Holocene (~10500 to ~1100 years BP) tephra fallout deposits (Table 1), at least two of them were > 5 in magnitude according to the Pyle (2000) scale, and three of them produced coarse-grained deposits generated by Plinian columns with heights exceeding 20 km (Watt et al., 2011). Prior to 2015, 11 historical eruptions have been reported since 1792, three of them having a Volcanic Explosivity Index (VEI; Newhall & Self, 1982) ≥3. Commonly, in the previous eruptions, lava flows, tephra fallout, PDCs and lahars characterized Calbuco's activity (Petit Breuilh, 1999; Moreno et al., 2006; Castruccio et al., 2010). Its last major eruption in 1961 developed a volcanic plume of ~12 km height and produced ~0.07 km^3 dense rock equivalent (DRE) (~0.2 km^3 bulk) of tephra (Romero et al., 2013), affecting the northeast sector of the volcano, including the city of Bariloche in Argentina (González-Ferrán, 1995; Petit-Breuilh, 1999, Daga et al., 2014).

In this work, we reports on the stratigraphy, grain size, clast density, total erupted volume, emplacement dynamics and eruption source parameters (ESP) like the column height and eruption duration of the tephra fall deposits associated with the 22-23 April 2015 eruption. We also present a preliminary petrological and geochemical characterization of the erupted rocks.

2. Calbuco volcano and the 22-23 April 2015 eruption

2.1 Volcanic evolution and historical activity

Calbuco volcano (Fig. 1A, B) is an active, truncated-cone composite stratovolcano (Moreno & López-Escobar, 2004), covering an area of 150 km² (Lahsen et al., 1985), which has been built during the last ~300 ky (Sellés & Moreno, 2011). Its evolution can be divided into four stages; Calbuco 1 (ca. 340-110 ky), which consists of abundant basaltic andesite and minor basaltic and andesitic (50.5-56.6 % SiO_2) lavas and volcanic breccias (Lahsen et al., 1985; Sellés & Moreno, 2011); Calbuco 2 (110-~14 ky), a sequence of glacially-eroded andesitic to dacitic (56-61% SiO_2) lavas interbedded with thick breccias from block-and ash-flow and lahars (Sellés & Moreno, 2011). At least two main edifice sector collapses occurred during the Holocene (Clavero et al., 2008). In particular, the 14 ky lateral collapse produced a volcanic avalanche of 2-3 km³ in volume that covered an area of ca. 55 km² in north-northwest direction, reaching a maximum thickness of 200 m and forming an elliptical caldera open toward the north-northeast (Lahsen et al., 1985; Petit-Breuilh & Moreno, 1997; Sellés & Moreno, 2011). During Calbuco 3 (ca.<14 ky to Holocene) the activity was located inside the caldera of Calbuco 2, with effusion of andesitic to basaltic andesite (54-60% SiO_2) and dacitic (64.5% SiO_2) lavas, plus PDCs, which were distributed toward the southern and northern sectors of the volcanic edifice (Sellés & Moreno, 2011). The Calbuco 4 (historical eruptions, <1893 AD) consists of a series of basaltic andesite to andesitic (54.8-59.3% SiO_2) blocky lava flows, a lava dome (growing in 1893, 1911-12 and 1917), block and ash flows, PDCs, tephra falls and lahars (López-Escobar et al., 1995; Sellés & Moreno, 2011). According to Petit Breuilh (1999), explosive eruptions occurred in 1792, 1845, 1893, 1894-95, 1906-07, 1917, 1927, 1929, 1932, 1945, 1961 and 1972. The highest intensity historical eruption of Calbuco occurred in 1893 and was widely registered in historical accounts (eg. Pöhlmann, 1893; Fisher, 1893; Martin, 1895; González, 1898; Steffen, 1909, 1944; Kinzel & Horn, 1983; Held, 1993),

producing tephra fallout, PDCs and hot lahars. Eruption columns reached a maximum height of 12 km above the crater level (acl) and were emitted on 19 April, 5 September, 5 October and 19 November 1893 (Petit Breuilh, 1999). Before the 2015 eruption, the previous major eruption occurred ~9 months after the 1960 M 9.5 Valdivia earthquake (Calbuco is 360 km distant from the 1960 earthquake epicentre), and lasted 3 months (Klohn, 1963; González-Ferrán, 1995; Petit Breuilh, 1999).

2.2 Chronology of the 2015 eruption

The 2015 eruption chronology is here summarized according to the Servicio Nacional de Geología y Minería (SERNAGEOMIN) reports. From 2010, when the volcano monitoring started at Calbuco, and until 2014 a total of 108 earthquakes occurred, of these 58 were interpreted as volcano-tectonic (VT) events and 50 as long-period (LP) events, and this background level of seismicity was characterized by LP events whose Reduced Displacement (RD) was <8 cm^2 (Valderrama et al., 2015). From 1 January to 21 April 2015 147 earthquakes (of these 142 VT) occurred at Calbuco (Valderrama et al., 2015), indicating a notable increase in seismic activity months prior to the eruption. On 22 April at 18:11 GMT (15:11 local time) a seismic swarm of 144 VT and LP events occurred below the east flank of the volcanic edifice (SERNAGEOMIN, 2015a). A thermal anomaly (<3 km distance from the crater) was evident on the satellite GOES-13 3.9 µm shortwave IR image at 20:45 GMT (20 minutes before the eruption onset). The hottest 3.9 µm IR brightness temperature at that time was 340.8 K, which is near the saturation temperature of the GOES-13 3.9 µm detectors (CiMMS, 2015). Hybrid seismic events reached RD values of 15.654 cm^2 10 minutes before the eruption onset (Valderrama et al., 2015). After this short-lived precursory activity, a surprisingly

intense explosive eruption was observed. The first pulse started at 21:05:55 GMT and lasted as a sustained eruption until 22:32 GMT producing an eruption column of ~15 km above the crater level (acl) (SERNAGEOMIN, 2015b). After an increase in seismicity at 00.20 GMT, which was characterized by hybrid and tremor signals with respective RD values of 75 cm^2 and 500 cm^2 (Valderrama et al., 2015), a second and more energetic phase started at 04:08 GMT on 23 April, and developed an eruption column of >15 km which was initially dispersed toward the northeast, lasting for 6 hours (SERNAGEOMIN, 2015c). The coldest, cloud-top IR brightness temperatures of both eruption pulses were -65.0 °C and -68.0 °C, and the column was approximately 18-20 km in height above sea level and 16-18 km acl (CiMMS, 2015). Although no pre-deformation was measured by interferogram up to 1-1/2 days before the eruption, a ~12 cm co-eruptive deflation was measured by the *Sentinel-1* interferogram on 26 April 2015, corresponding to a volume change of 0.054 km^3 about 5 km southwest of the volcano at a depth of 9.3 km (Delgado et al., 2015). Discrete ash emissions with columns <2 km in height occurred after this last phase on 23 April, including a third pulse which generated a 4 km high column with dispersion of tephra toward the southeast on 30 April.

3. Methods

3.1 Field mapping and dispersal reconstruction

The tephra investigation consisted of measuring deposit thickness and maximum clast sizes and sample collection in situ. All the sample sites were studied as soon as possible, between 23 April (after the end of the second phase) and 11 June 2015, in order to avoid surface erosion and reworking of the deposits. Collaboration from the people living in

areas affected by ash fallout through the media (facebook, twitter and email) was essential for collecting 26 thickness measurements on 23 April in distal areas of Chile (Fig. 1A). People collected data according to the following instructions: 1) collect samples after the end of ash fall; 2) measure tephra over plane surfaces in protected areas where no possibility of reworking of the deposit occurred; 3) accompany observations with photos containing objects of known dimensions (e.g. coin, pencil) and 4) send georeferenced data. Tephra field surveys were carried out in Chile and Argentina. A total of 21 distal (>27 km downwind) points were collected from 24 to 26 April in the Patagonia Argentina (Fig.1A), near Piedra del Águila, Junín de los Andes, San Martín de los Andes, Bariloche, Villa la Angostura, and Cardenal Samoré International Pass. Another 18 sites were sampled during two field campaigns on 6 May and from 4 June to 11 June at sites within a distance <27 km from the volcano (Fig. 1A, B). Overall, a total of 65 tephra fallout measurements are presented in this work (Fig. 1A, B). These field data were used to reconstruct the distribution of each recognized tephra fall layer. In addition, the dispersion of ash clouds was described with weather satellite images acquired on 22 and 23 April 2015 by the Geostationary Operational Environmental Satellite (GOES 13; http://cimss.ssec.wisc.edu/goes/blog/archives/date/2015/04/23), with the objective of comparing the deposit distribution with observation of the eruption cloud.

3.3 Tephra volume calculations

The deposit distribution was reconstructed using thickness measurements of each tephra layer. The areas of hand-drawn isopachs were measured using GIS software. The integration to compute tephra volume under the isopachs was performed using the

Exponential Thinning (Pyle, et al., 1989; 1995), Power Law (Bonadonna & Houghton, 2005) and Weibull models (Bonadonna & Costa, 2012). In the case of the Power Law method, we used as proximal limit of integration 1 km, and distal limits of 30 km (for units A and D) and 50 km (for units B and C). In addition, as Bonadonna & Costa (2012) suggested for the Weibull model, we used initial ranges for thickness scale (Θ), characteristic decay length scale of deposit thinning (λ) and n (shape parameter, dimensionless) of 0.1-5000 cm, 0.1-1000 km and 0.2-2, respectively.

3.4 Tephra characterization

Tephra fall deposit grain size was characterized using the parameters of Folk & Ward (1957), which were calculated with the Gradisat package (Blott & Pye, 2001). Sieving was performed for three representative samples downwind (DF10, DF05 and DF08) in the range -7.0 to 3.0 phi (Φ), where $\Phi=-\log_2 D/D_0$,and D is the particle diameter and D_0 is a reference diameter (1 mm). The stratigraphic correlation of the tephra layers has been done on the basis of lithology, componentry, grain size and color at most of the proximal to medial sites (5-27 km downwind), and by color changes in distal (>27 km in distance) areas.

The whole rock mineralogical composition was analyzed by X-ray diffraction (XRD), using a PAN analytical X-ray diffractometer (at 40 kV and 45 mA current), collecting data between 5 and 60 2Θ (2Θ is the total change in angle of the incoming electromagnetic wave) (Grupo de Caracterización de Materiales, Centro Atómico Bariloche). For referring to minerals, we used the Whitney & Evans (2010) abbreviations in all the analyses.

Preliminary analyses to determine the juvenile material bulk rock compositions were performed at the School of Earth, Atmospheric and Environmental Sciences of the University of Manchester (Manchester, UK), using the X-Ray fluorescence (XRF) spectrometry technique. The PAN analytical spectrometer, characterized by wavelength dispersive (WDXRF) systems, was used to analyze the bulk composition of the pumices. This instrument works with the Rh anode x-ray tube and it was configured for general geochemical analysis of rocks.

The mineral assemblage and textural features of pumices were observed using an optical microscope.

3.5 Eruption parameters

We measured the relative density of 27 clasts (size ranging from 0.7 to 5.3 cm in diameter) using a laboratory pycnometer filled with distilled water. Isopleth maps were reconstructed measuring the three largest clasts using the geometric mean of their 3 axis, as recommended by Bonadonna et al. (2013).

4. Tephra fall deposits of the 22-23 April eruption

4.2 Tephra stratigraphy

A summary of the most representative features (e.g. thickness, largest fragments, componentry and grain size) of the collected samples can be found in Table 2. Five tephra layers have been recognized within the eruptive sequence (Layers A, B, B1, C, and D). Nevertheless, B1 has been observed only in outcrop DF07. In the proximal

regime, which extends <15 km downwind (Table 2), the sequence starts with gray to brown layer A, showing a reverse grading. At site DF-10 (Table 2) layer A consists mostly of low-density, vesicular and light gray to light brown pumice clasts (LDP) (~80-~90%), high-density, poorly vesicular gray to brown pumice clasts (HDP) (~10-~20%) and rare lithics (~0.2%). Both pumice types are coarse lapilli in size. Lithics are not larger than 2 cm in diameter. The sequence continues with layers B and C, being normally graded and ungraded, respectively. At site DF-10 (Table 2) B and C are composed of brown, coarse lapilli to bomb sized clasts, whose components are in similar proportion as in layer A. Finally, the uppermost layer D is mostly made of HDP (~90%), LDP (~10%) and rare lithics (~0.2%), and has a distinct gray color. The layer is ungraded. A unique outcrop was found (13 km on 62° azimuth from the vent), which consists of the full eruptive sequence. Here Layer A is characterized by a total thickness of 19 cm, while layer B is interbedded by a high-density pumice layer (B1) of ~0.5 cm in thickness. No samples were collected from this site due to the difficulty of sampling layer B1 owing its reduced thickness.

The medial-distance (15-27 km from the vent) outcrops are characterized by a stratigraphic sequence formed by coarse ash to fine lapilli comprising layers B, C and D. Here, it is still possible to measure the thickness of each layer, although the full sequence is only 6-13 cm thick. The representative site DF05 (Table 2) shows an eruptive sequence formed by layers A, B, C and D. In this outcrop the contact between C and D is mostly gradational, and the concentration of HDP particles increases. As observed in other medial sites, this sequence is composed of layers C and D, which is dominated by HDP clasts. The farthest medial-distal outcrop in the downwind direction is represented by DF08 (27 km from the volcano, Table 2). Here, the sequence is

composed by coarse ash and layers B, C and D can be distinguished. Their thicknesses are, respectively, 1.5, 4.5 and ~0.5 cm.

At distal sites (>27 km downwind, Fig. 2A) the deposit varies from a single ash layer to a multiple-layered sequence that never exceeds 3 thin layers, which are formed mostly by fine to coarse ash-sized fragments. At some outcrop locations in Argentina, such as Collón Cura (Fig. 2B), the total deposit is 1.5 cm thick and is formed by layers B, C and D composed by fine ash. Stratigraphic variability is observed at Ruta 40 (Fig. 2C), Villa La Angostura and Cardenal Samoré international pass (Fig. 2D). Because the total deposit thickness, composed of medium to coarse ash, ranges from 0.4 to 0.5 cm, layers C and D are consistently distinguishable on the basis of change in color, but only in Samoré does the sequence start with layer B (Fig. 2D). As in most of the distal downwind deposits, layer A is not observable. Tephra thinning makes it difficult to measure and sample single ash units. Because of this, only total thickness measurements were performed at these outcrops. In other cases, along the downwind axis in Chile and Argentina, the deposit varies from a millimeter thick to a nominally assigned value of 0.1 mm, to represent trace quantities of ash. The same criterion of 0.1 mm was used to define trace ash deposition in Watt et al. (2009). At Pucón (Fig. 2E), Riñinahue (Fig. 2F) and Ralún (Fig. 2G) in Chile the deposit varies from 0.1 to 0.4 cm. Even where layers are not distinguishable, the evident difference in the ash color probably indicates that in the Chilean sites only layers B-C were deposited, with the exception of the Ralún site where the grey color suggests the presence of Layer D material. Most distal deposits found at other sites, such as Bariloche (Fig. 2H), Concepción (Fig. 2I) and Neuquén (Fig. 2J), consists of only a thin film whose coverage varied from partial to total, and a maximum thickness of 0.1- 1.0 mm was estimated.

The downwind outcrops show a progressive decrease of thickness away from the vent, and the most important feature in the sequence is the disappearance of layer A at a distance of > 26 km from the vent (Fig. 3A-A'). At Paso Cardenal Samoré (95 km from the vent), layer A is not present, layers B and C are very diffuse and it is not possible to establish a limit between them. These layers are thicker than layer D whose thickness has decreased considerably (~1.5 mm) (Fig. 3A-A'). The crosswind pits (Fig. 3B-B') are characterized to the northwest by the existence of a thin coarse ash fall, with a thickness of <1 cm in DF09-1 which is very diffuse, making difficult a subdivision in additional layers. An evident gray color to the top probably indicates the presence of layer D. The thickness of the deposit rapidly increases up to 13 cm near the downwind axis, being this sequence formed by layers A, B, C and D (Fig.3B-B'). Along the crosswind profile, we found DF07 which yields a total thickness of 19 cm and shows a full sequence formed by layers A, B, B1, C and D. Here layer B1 appears, but it is not observed in adjacent outcrops such as DF06, which is just 4 km from DF07 along the crosswind axis (Fig.3B-B'). The thickness of the deposit decreases rapidly to 6 cm in DF06 and layer A disappears. In contrast, layer D is thicker than B and C. Finally, the deposit becomes a single thin (0.2 cm) layer of ash in CB42, probably associated with layer D, as indicated by its grayish color. This suggests that the dispersion of D was mostly to the east rather than northeast, which is the case of layers A, B and C.

4.2 Tephra dispersal, distribution and volumes of tephra deposits

The plume image was captured by satellite GOES-13 on 22 April at 21.38 GMT just 33 minutes after the start of the eruption (Fig. 4A). The satellite image shows the expansion of the cloud toward the northeast on an azimuth of 48° (Fig. 4B). The plume detached

from the source at 23.08 GMT, indicating the end of the first phase of the eruption, and then dispersed over Argentina. After a period of rest between 22.33 and 04.00 GMT, a second plume started growing at 04.08 GMT (Fig. 4C) on 23 April and dispersed on an azimuth of ~55° (Fig.4D). At 06.35 GMT both the first and second plume coexisted between approximately 37°S and 41°S, due to a change in wind direction that caused the rotation of the first plume, dispersing the floating ash towards the northwest over southern Chile and western Argentina (Fig. 4E). The second plume became more elongated near the source at 09.38 GMT (Fig. 4F), probably due to a drastic decrease in the intensity and a minor change in the dispersal direction to azimuth ~67°. This plume left the source at 10.08 GMT on 23 April, being dispersed over Chile and Argentina. The cloud persisted over the region 37°S to 39°S between 11.45 and 16.00 GMT (Fig. 4G), as observed with the first plume (Fig. 4E).

The distal deposit distribution has been reconstructed for the total stratigraphic sequence using 47 field measurements taken in Chile and Argentina (Fig. 5A). The ash fall limit (0.01 cm thickness) has been hand-drawn using 12 measurements in Chile and Argentina. In that context, the southeastern limit of this finest ash was not measured in the field; rather it has been extrapolated by using satellite images acquired on 25 April (Fig. 5A). In comparison, with a total of 19 measurements we reconstructed the isopach maps by hand-drawning for the total deposit in the proximal to medial area (Fig. 5B), and for individual layers A, B, C and D (Fig. 5C-G). Due to paucity of field data, we did not reconstruct an isopach map for layer B1. The deposit thins with distance with exception of an outsider region near Piedra del Aguila and Collón Cura river, both in Argentina (represented by CB03 and CB06, respectively in Fig. 5A), which represents a secondary thicker region (Fig. 5A). The non elliptical shape of the total deposit at distal

locations (Fig. 5A), and also the secondary thicker region could be related to the plume complex dispersal during the eruption (Fig. 5E, 5G) and it is discussed in Section 5.

Isopach maps of individual layers (Fig. 5C-6F) show that, during the first phase of activity, layer A is aligned on an azimuth of ~47° and is not identified at a distance beyond 15 km from the vent (Fig. 5C). Layer B has an elliptical deposition pattern along an azimuth of ~42° and extends considerably further than layer A (Fig. 5D, 5E). The distribution of layers A and B are in good agreement with the plume dispersion during the first pulse of eruption, suggesting that both layers were formed during that stage. Layer C has an elliptical shape with dispersal axis of azimuth ~50° (Fig. 5E), which is similar to the plume axis observed during the start of the second pulse of the eruption. Layer C thins from 25 cm to ~3 cm over a distance of 27 km downwind. Finally, layer D thins gradually along its axis toward the east (~71° azimuth) and is more elongate relative to layers B and C (Fig. 5E, 5F).

We calculated tephra volumes (Table 3) using the thinner isopach mapped of each layer, which is 2 cm in the case of layers A, B and D, and 3 cm for layer C. Because no data have been obtained for individual layers in distal regions, we assume that the integrated volumes only reflect proximal and medial thinning trends of these deposits. The range of volume estimates, obtained from the Exponential (Pyle, et al., 1989; 1995), Power-Law (Bonadonna & Houghton, 2005) and Weibull techniques (Bonadonna & Costa, 2012), measured in units of 10^{-3} km^3 for each layer are: A) 8.61-21.6; B) 30.9-34.0; C) 50.3-64.3; D) 9.6-37.1. The considerable variability of results of the Weibull method, specially for calculations of layers A and D, can be attributed to the lack of distal data, which may result in a discrepancy of 99% (Bonadonna & Costa, 2012). The sum of integrated individual volumes for each layer, using the different methods (Table 3), for proximal and medial data, yields a bulk volume that ranges from 0.105 to 0.14 km^3. If

the same methods are applied for the total deposit thickness data in all locations (including distal, >27 km downwind from the vent), we estimate the bulk volume (Table 3) to range from 0.267 to 0.277 km^3. Using a bulk deposit density, measured from four fine-grained lapilli samples, of ~997.3 kg m^{-3}, we estimated the deposit mass to be 2.66-2.76 x 10^{11} kg. Assuming a proportion of 80% LDP and 20% HDP, with density of 2450-2500 kg m^{-3} for a basaltic andesitic magma, we calculate a deposit dense rock equivalent (DRE) of ~0.11-0.13 km^3.

4.3 Physical features of ejected material

4.3.1 Grain-Size

At the most proximal outcrop DF10 the basal layer A shows a polymodal (Fig.6A) and poorly sorted distribution of coarse lapilli particles. Three modes are identified: -4.0, -2.9 and -2.13 Φ. As observed in other eruptions, the existence of several modes for the grain size distribution of the tephra deposits at a few kilometers from the vent is due to pronounced differences in density between pumice, crystals, and rock fragments (Fisher & Schmincke, 1984). Layers B-C are composed of coarse lapilli and some bomb-sized fragments, forming poorly sorted distributions with notable modes at -4.3 and -2.6 Φ, respectively. Layer D has finer grains with modes at -2.9,-2.13 and 2.0 Φ.

In the medial distance site DF05 the grain size is smaller than at DF10 (Fig. 6B). Layers A and B-C are polymodal and poorly sorted, while layer D is polymodal and moderately sorted; A, B-C and D modes are at -2.13, -1.38 and -0.13 Φ.

Site DF08, which marks the limit between the medial-distal outcrops, includes layers B-C and D, which were sieved at 0.24 Φ steps (Fig. 6C); they present well sorted

unimodal distributions with a single mode at 0.75 Φ. Distal and very distal samples were not sieved by layer, because of their limited thickness did not allow us to perform a sampling. Meanwhile, a laser grain size analysis (< 63 µm fraction) of the whole deposit collected at CB30 (Bariloche, Argentina) shows a unimodal, very well sorted and almost normal distribution with a mode at -4.8 Φ (Romina Daga, personal communication).

A reverse size grading is common in layer A; in contrast, layers B and C represent the thickest part of the profile and are very uniform in componentry, grain size distribution, and the presence of normal grading. No grading is observed in layer D.

4.3.2 Tephra petrography and mineralogy

The eruption produced two types of pumice clasts: HDP is poorly vesiculated and crystal-rich (up to 40 % crystals by volume), whereas LDP is characterized by lower crystallinity due to the higher vesicle volume fraction. Banded pumice clasts are quite common in layers A, B and C, and their bands consist of both high-density and low-density pumice. Denser pumice clasts are most common in layer D. The presence of bands is related to areas with different vesicle volume fractions within the pumice. Textural features and mineralogical assemblages of dense (Fig. 7A and B) and vesiculated (Fig. 7C and D) pumices are constant for each layer. From a petrographic point of view, pumice clasts are characterized by porphyritic textures with no evidence of anisotropy: in fact, crystals and vesicles are not preferentially oriented with respect to a possible magma flow direction (Fig. 7). Crystal textures include phenocrysts in a glassy groundmass with a minor presence of microlites. The mineralogical assemblage of pumice consists of plagioclase (plg), orthopyroxene (opx), clinopyroxene (cpx) and

Ti-magnetite (ox) (quartz is present as accessory phase). The size of these mineral grains ranges between ~100 µm and ~1 mm, but microlites of a few microns (from <1 to 30 µm) are also present in the glassy matrix, and their assemblage consists of plg, opx, cpx and ox. Occasionally, a glomeroporphyritic texture is observed, with aggregates consisting of plg, cpx and opx (Fig. 7B and C). Normal zonation in plg phenocrysts is also observed. Preliminary XRF analyses show that the bulk compositions of these samples correspond to porphyritic basaltic andesites (~55 wt.% of SiO_2). The groundmass composition of these samples has not been analyzed in details yet, however, the first results indicate that it is a dacite (~66 wt.% of SiO_2; Astudillo et al., 2015).

An ash sample suite collected at San Carlos de Bariloche, Argentina (100 km E from Calbuco) around 10:30 GMT on 23 April, was analyzed using XRD (see Methods). This sample contains material emitted during the two main pulses, because their deposition occurred during the night of 22 April and early morning of 23 April, resulting in a millimeter-thick deposit. At that time, the sky was cloudy and only very fine 'dust' was perceptible in the atmosphere, producing an ash trace over the trays. This fine-ash sample contains abundant crystal fragments and lithic clasts, and a low amount of volcanic glass. Main accessory phases include plg, opx and cpx. The glassy material occurred as vesicular and blocky particles in the coarse fraction (~200 µm) and as angular, dense shards in the fine fraction.

Observations of the < 63µm fraction of the proximal-medial KAL-18 and KAL-21 samples for layer B (Table 2), indicate that the ash is gray and composed by vitreous and crystalline fragments. Vitreous fragments are mainly blocky, angular and compact glass shards, and occasionally exhibit starry bubble walls. Free crystals are angular to sub-rounded, with abundant plg, px and a minor quantity of quartz. Within the same

sample but in layer C, the < 63µm fraction contains more free crystals relative to layer B; the mineral assemblage is similar. In addition, the ash of layer C is clear brown.

4.4 Eruption parameters

In addition to crystallinity and vesicularity, which have allowed us to discriminate well between the two types of pumice (LDP and HDP), measurement of clast densities has confirmed the bimodality of juvenile particles. The analyzed fragments consisted of 14 LDP, 9 HDP and 4 lithic samples. The average density of LDP, HDP and lithic clasts has been calculated as 760±0.23, 1670±0.25 and 2190±0.39 kg m^{-3}, respectively. The LDP and HDP clasts differ at least in the amount of vesicles, as observed in the samples. In contrast, lithics have uniform density and vesicularity is low.

We measured the three largest (or maximum size) clasts of layers A, B-C and D: 8 maximum LDP (MLDP), 8 maximum HDP (MHDP) and 6 maximum lithics (ML). With clast density data, we applied the model of Carey & Sparks (1986) to estimate the plume height above the vent in km (Table 4). Computed column heights are considerably smaller (9.0-14.5 km) when a density of 760 kg m^{-3} is used (MLDP), in contrast to the results obtained using denser clasts (MHDP and ML), which give higher values (12 to 15.4 km height). Bonadonna et al. (2013) suggest that pumices are not recommended for this procedure, because these fragile fragments can be broken during the impact with soil. For this reason, we prefer the results calculated with MHDP and ML fragments (1670 or 2190 kg m^{-3}). Using the method of Carey & Sparks (1986) and assuming a density of 1670 kg m^{-3}, we calculated the MHDP of 2.4 cm diameter for layers B-C. The inferred isopleth of the MHDP reported in Table 2 was used to compute a column height of 15.4 km, which is similar to that reported by eyewitness observation

(SERNAGEOMIN, 2015b, c). Similarly, the values calculated for the column heights associated with layers A and D are respectively 10.2-12.3 km and 11.8-13.2 km.

When the average total erupted mass (TM, kg) of units B-C is considered, and the column height equation of Sparks et al. (1997) is solved for mass discharge rate (MDR), we can calculate the duration of the eruption as TM/MDR, which yields an estimate of 4.67 h (Table 4). In the same way, the eruption durations for layers A and D are estimated to be 0.54-1.03 h and 1.79-2.76 h, respectively (Table 4). In this context, the full eruption duration (all layers, both pulses) is calculated between 7 and 11 hours. Official reports indicate that the first pulse lasted 1.5 h and the second 6 hours, so the total duration was 7.5 h. This allows us to discriminate among these calculations and to consider that the most plausible eruptive scenario corresponds to columns varying from 12 to 15.4 km, with a total duration of the eruption of about 7 hours (Table 4). Our total mass and MDR values can be used to estimate the magnitude and intensity of each unit, following the approach of Pyle (2000). Individually, magnitude varies from 3.0 to 4.14, and it is 4.45 for the total deposit (Table 5).

5. Discussion

5.1 Eruption dynamics

In this study we have divided the stratigraphic sequence of the 22-23 April 2015 eruption into several layers, which can be individually sampled and measured only in the proximal-medial deposits. In distal areas, these layers could not be measured, sampled or correlated with accuracy. Because of this, our stratigraphic characterization of layers is based on the study of proximal to medial outcrops. Size grading is most commonly interpreted in terms of steadiness of the eruption column, but can also be

influenced by wind shifts and inclination of the column or jet (Houghton & Carey, 2015). The size grading shown by our tephra layers lead to the interpretation that layer A represents the start of the eruption, with a progressive increase of intensity, followed by a paroxysm of activity at the A-B transition, which was followed by a sustained eruption at layer C and waning of the eruption represented by the non-graded layer D (Fig. 8). According to the results obtained with the largest clast data, an average column height of ~15.4 km has been estimated for layers B and C, which aligns with observations given in official reports (SERNAGEOMIN, 2015b, c). Our calculations of column height give smaller values compared to satellite imagery that indicate a column of 16-18 km in height (CiMMS, 2015). An intrinsic uncertainty of at least ±20 % has been reported for the Carey & Sparks (1986) method for column height estimation (Biass & Bonadonna, 2011); therefore, we consider the maximum column height to have been in the range 15.4 ± 3.08 km for layers B and C. In any case, the largest values of column height in B and C suggest the occurrence of two strong energy episodes. This suggests difference in wind direction that could be related to variation in the meteorological conditions or a change in the column height.

Additionally, layers B and C show a very similar deposit distribution on land (Fig. 5D, E), and both the first and second pulse plumes were dispersed in very similar directions according to satellite imagery (Fig. 4). In fact, a similar dynamics of layers B and C may indicate rising of two paroxysmal phases at the end of the eruption onset and during the start of the second pulse on 22 and 23 April 2015 (Fig. 8), respectively. Good agreement is found when the satellite image of the 09.38 GMT on 23 April is compared with the dispersal of layer D.

A sharp distinction in grain size among layers in fallout deposits is commonly interpreted as non-sustained or spasmodic activity (Houghton & Carey, 2015);

therefore, the field observations of the 22-23 April tephra deposits imply that the eruption which deposited these layers was likely sustained (Fig. 8), although two distinct pulses deposited the whole sequence. The evident gradual contact seen at medial-distal distance, especially between layers C-D, makes it difficult to delimitate layer thickness. Such contact may be explained in terms of the higher density of the particles of the D layer plume, which probably fell together with some of the C layer particles because of the higher settling velocity of the denser particles in the D tephra (Bonadonna et al., 1998). Also, direct observations indicate that there was not a pause between the emission of C and D tephras, which indicates that the eruption evolved progressively with time, with a decreasing eruptive column height ranging from ~15.4 to ~12-13 km (Fig. 8). This is also supported by satellite observations of the plume, which became elongated near the source at 09.38 GMT (Fig. 4F), before detaching from the source at 10.08 GMT on 23 April.

The DF07 site (Table 2) is the most difficult to explain because a thin (0.5 cm), high-density pumice layer (B1) is observed to interrupt layer B. This outcrop is located 13 km from the vent and at an azimuth of 62° (Fig. 2D); layer B1 does not appear in other crosswind sections investigated (Fig. 3). In comparison to B1, layer B has a considerable difference in the dispersal axis with an azimuth of ~42°. From these observations, we suggest that B1 was deposited before the end of the first eruptive pulse on 22 April and only in a very narrow strip of land. According to oblique photos from ground-based observers, before the end of the first eruption pulse, a low-altitude (~2-3 km acl) secondary plume arose from the vent and was dispersed to ~60° azimuth (Fig. 8). Some possible explanations for this phenomenon are, for example, an atmospheric stratification transporting denser fragments in a specific altitude level, or more likely the activity of multiple vents emitting different materials simultaneously. Rapid satellite

imagery acquisition after the eruption on 25 April (https://www.disasterscharter.org/web/guest/-/volcano-in-ch-20) reveals venting from six craters and field photography show almost two individual lava fountains (Fig. 8).

The total deposit isopach map also provides insight of a secondary thickness maxima observed approximately 150 km downwind from the vent. This feature was attributed to particle aggregation process in the tephra fall deposits of Mt. Hudson 1991 eruption (Scasso et al., 1994) and Mt. Saint Helens 1980 eruption (Durant et al., 2009). Recently, Watt et al. (2015) reported two possible causes for a secondary thickness maxima at the Cha1 Plinian tephra deposit of Chaitén volcano. These include the formation of liquid pellets driven by rainfall, or more likely an accelerated deposition of particles (100 to 500 µm) influenced by topography of the downwind regime. Our results do not include grain size analysis in that area, but according to satellite observations we suggest that an overlap of the different eruption plumes of each pulse may have influenced the deposition of thicker tephra layers over the 37°S-41°S as observed in other eruptions (e.g., Watt et al., 2009), in this case due to a change in wind direction. An investigation on topography-controlled deposition and aggregation of particles have to be object of a detailed study in the future, especially because these tephra secondary thickness maximum regions may have a larger impact for tephra fallout.

The complexity of deposits emplaced by multiple vents and PDCs, possibly produced by several mechanisms (e.g., partial column collapse, lateral jetting), suggest that the stratigraphic sequence may be much more complex close to the vents than we were able to sample (ca. 5 km). More sampling in areas close to the vent would be useful for a better reconstruction of proximal stratigraphy and eruptive mechanisms. According to eyewitness observations, the column collapse started at the end of the first pulse (here top of layer B); our observations, however, are based on tephra fall deposits and we did

not collect samples for characterizing PDCs. Future investigations should be focused on the stratigraphic correlation between the tephra fall sequence and PDC deposits, in order to achieve a better reconstruction of the explosive eruption dynamics. In addition, detailed petrological and geochemical studies of the erupted material are required for understanding the pre-eruptive conditions of this sudden eruption.

5.2 Eruption style

Our volume estimates are not absolute values, because an inherent uncertainty is intrinsically related to the measuring procedure, isopach drawing technique and method of integration (e.g. Bonadonna & Costa, 2012; Andrónico et al., 2014; Klawonn et al., 2014; Bonadonna et al., 2015). Layers B, C and D are observed in distal sections, so we assume that the distal deposit is made almost exclusively of these three layers. These thin (<1 cm) deposits do not allow for an accurate measurement of single layers. Our best estimate is that layer A accounts for ~11% of the total volume, B contributes ~27.4%, C ~46% and D 15.6 %. Using these volume estimates, weighting them by the proportion of each layer and the total volumes calculated including distal data, we obtain the volume equivalences for each model and layer of the whole deposit (proximal to distal) (Fig. 9A). Therefore, the first pulse released ~38% and the second pulse ~62% of the total volume. Acknowledging propagation of uncertainty, we refer to volume estimates in terms of ranges derived using different methods. Using our values and the volumes erupted based on 65 sample sites spanning proximal to distal sites, we calculate a cumulative trend in time based on each model (Fig. 9B). In terms of intensity, the layers range from 9.49 (unit D) to 10.34 (unit C), and the total deposit is 10.01 (Table 5). This implies that the Calbuco eruption can be classified as VEI 4. According to the

conventional classification scheme applied by Alfano et al. (2011) for the 2008-2009 Chaitén volcano eruption, the total deposit of this eruption plots in the field of Subplinian eruptions (Fig. 9C). This explosive eruptive behavior is similar to historic eruptions at Calbuco (for example in 1893-95; 1917; 1929; 1961), with the exception that the present eruption did not produce lava flows or lava domes. Furthermore, the tephra fall volume discharged by the 2015 eruption is similar to that calculated for the eruption of 1961 (~0.2 km^3; Romero et al., 2013). The ejecta basaltic andesitic composition is also very similar to that reported for previous eruptions in 1917, 1961 and 1971 by Sellés & Moreno (2011). If we consider that the historical records of Calbuco eruptions are dependable from the 1906 eruption (due to the human activity in the area), nine eruptions have occurred in the last 109 years (including 2015). Thus, the eruption rate is approximately 0.083 eruptions/year and the repose time (*1/eruption rate*) is near to 12 years. Even if the pre-eruptive seismic swarm started only a few hours prior the eruption onset (SERNAGEOMIN, 2015a) and no pre-eruptive deformation was observed (Delgado et al., 2015), the steady increase in seismicity three months before the eruption (Valderrama et al., 2015) would be sufficient for providing an early advice of volcanic unrest. Calbuco volcano is one of the most hazardous volcanoes of southern Andes. As a consequence of that, tephra fall hazard is a topic that needs to be addressed for southern Andean communities like it has been demonstrated by this eruption and other recent volcanic activity in this region (e.g. Wilson et al., 2010; Alfano et al., 2011; Araya, 2015; Elissondo et al., 2015)

6. Conclusions

The 22-23 April 2015 basaltic andesitic (~55 wt. % of SiO_2) eruption of Calbuco volcano started suddenly with a high-intensity explosive phase with very little warning to the neighbouring communities. Two main subplinian pulses separated by a few hours deposited five tephra fall layers, mostly northeast of the volcano. The first pulse started on April 22 at 21.05 GMT with a column ~15 km high above the crater and deposited layers A, B and B1. Layer B1 is interpreted as sedimentation of a secondary low-altitude plume. Another eruption pulse occurred on 23 April at 04.09 GMT with a column >15 km in height, and deposited layers C and D. The proximal stratigraphy reveals four of the five units, and most of the ejected products range from coarse lapilli to bomb-size. The deposits thin and particle diameter decreases with distance along the downwind axis, with the exception of an outsider region in Argentina (Collón Cura and Piedra del Águila), which is likely the result of variations in the wind pattern. These distal deposits consist of 2 or 3 layers (sometimes C-D or B, C and D) when they can be discriminated, but only a single ash trace is observed in most of the distal sampling localities in Patagonia Argentina and Southern Chile. The total volume of the eruption is estimated to be 0.28 km^3 of bulk tephra, which is equivalent to 0.11-0.13 km^3 DRE. The first phase released ~38% of the total volume with layer C accounting for ~46% of the total released tephra. Layer D accounted for 16% of the deposited tephra. The magnitude of the eruptions producing each layer ranged between 3.0 and 4.14 and the intensity from 9.49 to 10.34, while the whole eruption is 4.45 and 10.01 in magnitude and intensity, respectively. This was a VEI 4 eruption.

Acknowledgements

This work, was supported by the ERC Consolidator Grant 612776 – CHRONOS (D. Pergini) and the ERC Consolidator Grant 279802 – CO2_VOLC (M.Burton). The Authors acknowledge the editor L. Wilson and the two reviewers S. Watt and M. A. Di Vito for whose revisions greatly improved the manuscript. We would like to thank F. J. Swanson for constructive comments on the manuscript. Support from I. Boroni, Hermes G., A. Martinez, I. Silva, H. Moyano, R. Garrido, V. Astete and M. Lincopi was essential to obtain near real-time, geo-referenced data of tephra fall in distal areas. Photos from Roger Smith, C. Valenzuela, E. Minte, C. Barría, K. Horning and D. Spatafore helped to reconstruct the eruption chronology. Romero, Morgavi and Arzilli are grateful to Mr. F. Mancilla and J. Valenzuela (TerraSur Ensenada Corp.) for their assistance during fieldwork.

References

Alfano, F., Bonadonna, C., Volentik A.C.M., Connor, C.B., Watt, S.F.L., Pyle, D.M., Connor, L.J. 2011, Tephra stratigraphy and eruptive volume of the May, 2008, Chaitén eruption, Chile. Bull. Volcanol., 73, 613-630.

Andronico, D., Scollo, S., Cristaldi, A., Lo Castro, M.D., 2014. Representivity of incompletely sampled fall deposits in estimating eruption source parameters: a test using the 12-13 January 2011 lava fountain deposit from Mt. Etna volcano, Italy. Bull. Volcanol., 76: 861. DOI: 10.1007/s00445-014-0861-3.

Araya, O., 2015. Erupciones volcánicas. Efectos sobre la ganadería. Ediciones UACH, Valdivia, Chile.

Astudillo, V., Bertin, L., Bertin, D. 2015. Características texturales y composicionales de la tefra del ciclo eruptivo de Abril-Mayo de 2015 en el volcán Calbuco. In Congreso Geológico Chileno, No. XIV, La Serena, Chile.

Biass, S. & Bonadonna, C., 2011. A quantitative uncertainty assessment of eruptive parameters derived from tephra deposits: the example of two large eruptions of Cotopaxi volcano, Ecuador. Bull. Volcanol.73: 73-90.

Blott, S.J. & Pye, K., 2001. Gradisat: A grain size distribution and statistics package for the analysis of unconsolidated sediments. Earth Surf. Process. Landforms, 26: 1237-1248. DOI: 10.1002/esp.261

Bonadonna, C. & Costa, A., 2012. Estimating the volume of tephra deposits: A new simple strategy, Geology, 40 (5), 415–418. doi:10.1130/G32769.1

Bonadonna, C. & Costa, A., 2013. Plume height, volume, and classification of explosive volcanic eruptions based on the Weibull function. Bull. Volcanol., 75(8)

Bonadonna, C. & Houghton, B.F., 2005. Total grainsize distribution and volume of tephra fall deposits. Bull. Volcanol., 67: 441-456.

Bonadonna, C., Biass, S., Costa, A., 2015. Physical characterizationof explosive volcanic eruptions based on tephra deposits: Propagation of uncertainties and sensitivity analysis, J. of Volcanol. Geotherm. Res., doi: 10.1016/j.jvolgeores.2015.03.009

Bonadonna, C., Ernst, G. G. J., Sparks, R. S. J., 1998. Thickness variations and volume estimates of tephra fall deposits: the importance of particle Reynolds number. J. Volcanol. and Geotherm. Res, *81*(3), 173-187.

Carey, S., & Sparks, R. S. J., 1986. Quantitative models of the fallout and dispersal of tephra from volcanic eruption columns. Bull. Volcanol., 48(2-3), 109-125. DOI: 10.1007/BF01046546

Castruccio, A., Clavero, J., Rivera, A., 2010. Comparative study of lahars generated by the 1961 and 1971 eruptions of Calbuco and Villarrica volcanoes, Southern Andes of Chile. J. Volcanol. and Geotherm. Res, v.190 (n.3-4): pp.297-311

CiMMS Satelite Blog. Accessed on July 03, 2015. http://cimss.ssec.wisc.edu/goes/blog/archives/date/2015/04/23

Clavero, J., Godoy, E., Arancibia, G., Rojas, C., Moreno, H., 2008. Multiple Holocene sector collapses at Calbuco volcano, Southern Andes. Abstracts, Poster Session III, IAVCEI General Assembly, Reykjavik, Iceland, p. 41.

Daga, R., Guevara, S., Poiré, D.G., Arribére, M., 2014. Characterization of tephras dispersed by the recent eruptions of volcanoes Calbuco (1961), Chaitén (2008) and Cordón Caulle Complex (1960 and 2011), in Northern Patagonia. Journal of South American Earth Sciences, 49 (2014) 1-14

Delgado, F., Pritchard, M.E., Ebmeier, S., Biggs, J., Arnold, D., González, P., Poland, M., Zoffoli, S., Córdova, L., Lara, L.E. 2015. The CEOS pilot project, satellite volcano monitoring in Latin America and new InSAR ground deformation results at Llaima, Villarica and Calbuco volcanoes. In Congreso Geológico Chileno, No. XIV, La Serena, Chile.

Durant, A.J., Rose, W.I., Sarna-Wojcicki, A.M., Carey, S., Volentik, A.C.M., 2009. Hydrometeor-enhanced tephra sedimentation: constraints from the 18 May, 1980 eruption of Mount St. Helens. J. Geophys. Res. 114: B03204

Elissondo, M., Baumann, V., Bonadonna, C., Pistolesi, M., Cioni, R., Bertagnini, A., Biass, S., Herrero, J.C., Gonzalez, R., 2015.Chronology and impact of the 2011 Puyehue-Cordón Caulle eruption, Chile. Nat. Hazards Earth Syst. Sci. Discuss. DOI: 10.5194/nhessd-3-5383-2015

Fisher, O., 1893. Erupción del volcán Calbuco. Anales de la Universidad de Chile LXXXV: 197-204. Santiago, Chile.

Fisher, R. V., & Schmincke, H. U., 1984. Pyroclastic rocks, 472 pp. *Springer*, Berlin. doi, 10, 978-3.

Folk, R.L. & Ward, W.C., 1957. Brazos river bar: A study in the significance of grain size parameters. Journal of Sedimentary Petrology, 27: 3-26.

González, F., 1898. Exploraciones hidrográficas de la cañonera Pilcomayo en la costa sur de la república i Chiloé en 1893-94. Anuario hidrográfico de la Marina de Chile. Imprenta i encuadernación Barcelona, Año 21:45-118. Santiago, Chile.

González-Ferrán, O., 1995. Volcanes de Chile. Instituto Geográfico militar, Santiago, Chile.

Held, E. 1993. familia Held: antecedentes históricos. Radicación de Gottfried Held y familia en la colonia del lago Llanquihue. Antepasados en Alemania y descendientes en Chile. Claus von Plate: 314 p. Santiago.

Houghton, B. & Carey, R.J., 2015. Pyroclastic fall deposits. In Sigurdsson, H., Houghton, B., McNutt, S., Rymer, H., & Stix, J. (Eds.). (2015). *The encyclopedia of volcanoes*. Elsevier.

Kinzel, E. & Horn, B. 1983. Puerto Varas, 130 años de historia, 1852-1983. Puerto Varas, Chile, Imprenta y Librería Horn: 414 p

Klawonn, M., Houghton, B.F., Swanson, D.A., Fagents, S.A., Wessel, P., Wolfe, C.J., 2014. From field data to volumes: costraining uncertainties in pyroclastic eruption parameters. Bull. Volcanol., 76:893.

Klohn, E., 1963. The February 1961 eruption of Calbuco volcano. Bulletin of the Seismological Society of America v.53 (n.6): pp.1435-1963

Lahsen, A., Moreno, H., Varela, J., Munizaga, F., López, L., 1985. Proyecto Canutillar : geología y riesgo volcánico del volcán Calbuco y centros eruptivos menores. Universidad de Chile, ENDESA: 215 p.

López-Escobar, L., Parada, M.A., Hickey-Vargas, R., Frey, F.A., Kempton, P.D., Moreno, H., 1995. Calbuco Volcano and minor eruptive center distributed along the Liquiñe Ofqui Fault Zone, Chile -41º-42ºs-: contrasting origin of andesitic and basaltic magma in the Southern Volcanic Zone of the Andes. Contributions to Mineralogy and Petrology v.119: pp.345-361

Martin, C., 1895. La erupción del volcán Calbuco. Anales de la Universidad de Chile, Imprenta Cervantes: 161-193. Santiago.

Moreno, H. & Naranjo, J.A., 2004. Calbuco volcano historic block-and-ash and pyroclastic flows: increasing threatening on surrounding communities, Southern Andes 41.5ºS. In IAVCEI General Assembly, Pucón, Chile, November 2004: v.4

Moreno, H., Naranjo, J.A., Clavero, J., 2006. Generación de lahares calientes en el volcán Calbuco, Andes del Sur de Chile (41,3ºS). In XI Congreso Geológico Chileno. Antofagasta (CD).

Newhall, C., Self, S. 1982. The volcanic explosivity index (VEI): An estimate of explosive magnitude for historical volcanism. J. Geophys. Res., 87, 1231-1238.

Petit-Breuilh, M.E. & Moreno, H., 1997. La erupción de 1893-1895 del Volcán Calbuco -41.3ºS- y sus efectos ambientales. En Congreso Geológico Chileno, 8., Antofagasta, Chile, 13-17 Octubre 1997: pp.780-784

Petit-Breuilh, M.E., 1999. Cronología eruptiva histórica de los volcanes Osorno y Calbuco, Andes del Sur -41º-41º30'S. SERNAGEOMIN, Boletín (n.53): 46 p.

Pöhlmann, R., 1893. Estudio microscópico de algunas cenizas volcánicas del Calbuco, provenientes de las erupciones del año 1893. Anales de la Universidad de Chile, LXXXV: 204-217. Santiago.

Pyle, D. M., 2000. Sizes of Volcanic Eruption. Encyclopedia of Volcanoes. Academy Press. Part II, pp 263-269. San Diego California.

Pyle, D. M., 2000. Sizes of Volcanic Eruption. Encyclopedia of Volcanoes. Academy Press. Part II, pp 263-269. San Diego California.

Pyle, D.M., 1989. The thickness, volume and grainsize of tephra fall deposits: Bull Volcanol, 51, 1-15.

Pyle, D.M., 1995. Assessment of the minimum volume of tephra fall deposits, J. Volcanol. Geotherm. Res., 69, 379–382, doi:10.1016/0377- 0273(95)00038-0.

Romero, J.E., Viramonte, J.G., Scasso, R.A., 2013. Indirect tephra volume estimations using theoretical models for some Chilean historical volcanic eruptions with sustained columns. Bolletino di Geofisica teorica ed applicata, 54(Supplement 2):194-197.

Sellés, D., Moreno, H. 2011. Geología del volcán Calbuco. Carta Geológica de Chile, Serie Geología Básica No. 130, escala 1:50.000.

SERNAGEOMIN, 2015a. Reporte Especial de Actividad Volcánica (REAV) Región de los Lagos. (REAV) Año 2015 Abril 22 (20:45 HL)

SERNAGEOMIN, 2015b. Reporte Especial de Actividad Volcánica (REAV) Región de los Lagos. Año 2015 Abril 22 (22:30 HL).

SERNAGEOMIN, 2015c. Reporte Especial de Actividad Volcánica (REAV) Región de los Lagos. Año 2015 Abril 23 (10:30 HL)

Scasso, R.A., Corbella, H., Tiberi, P., 1994. Sedimentological analysis of the tephra from the 12–15 August 1991 eruption of Hudson volcano. Bull. Volcanol., 56:121–132

Sparks, R. S. J., Bursik, M. I., Carey, S. N., Gilbert, J. S., Glaze, L. S., Sigurdsson, H., Woods, A. W., 1997, “Volcanic Plumes”, John Wiley and Sons, New York, 574 pp

Sparks, R.S.J., Bursik, M.I., Ablay, G., Thomas, R.M.E., Carey, S.N., 1992. Sedimentation of tephra by volcanic plumes: Part 2. Controls on thickness and grain-size variations of tephra fall deposits. Bull. Volcanol. 54, 685–695.

Steffen, H., 1909. Viajes de esploración y estudio de la Patagonia occidental 1892-1902. Imprenta Cervantes: 409 p. Santiago

Steffen, H., 1944. Patagonia occidental. Las cordilleras patagónicas y sus regiones circundantes. Ediciones de la Universidad de Chile: 333 p. Santiago.

Stern, C., Moreno, H., Lopez-Escobar, L., Clavero, J., Lara, L., Naranjo, J., Parada, M., Skewes, M., 2007. Chilean Volcanoes. In: Moreno, T., Gibbons, W. (eds) The Geology of Chile, Geological Society of London, London pp 149-180

Valderrama, O., Franco, L., Gil-Cruz, F., 2015. Erupción intempestiva del volcán Calbuco, Abril 2015. In Congreso Geológico Chileno, No. XIV, La Serena, Chile.

Watt, S.F.L., Pyle, D.M., Mather, T.A., Martin, R.S. & Matthews, N.E., 2009. Fallout and distribution of volcanic ash over Argentina following the May 2008 explosive eruption of Chaitén, Chile. J. Geophys. Res.-Solid Earth 114:11. doi:B0420710.1029/2008jb006219

Watt, S.F.L., D.M. Pyle, J.A. Naranjo, G. Rosqvist., M. Mella., T.A. Mather, Moreno, H., 2011. Holocene tephrochronology of the Hualaihue region (Andean southern volcanic zone, ~42° S), southern Chile. Quaternary International 246, 324–343.

Watt, S., Gilbert, J., Folch, A., Phillips, J., Cai, X., 2015. An example of enhanced tephra fallout driven by topographically-induced atmospheric turbulence. Bull. Volcanol., 77 (35), doi: 10.1007/s00445-015-0927- x

Whitney, D. L., & Evans, B. W. 2010. Abbreviations for names of rock-forming minerals. American mineralogist, 95(1), 185.

Wilson, T., Cole, J., Cronin, S., Stewart, C., Johnston, D., 2010. Impacts on agriculture following the 1991 eruption of Vulcan Hudson, Patagonia: lessons for recovery. Nat. Hazards. DOI: 10.1007/s11069-010-9604-8.

Figure captions

Fig.1: Location map of Calbuco Volcano, showing the data points used in this study, and the most important cities in Chile and Argentina. The distal data points are included in **A**, and the proximal to medial points are in **B**.

Fig.2: Tephra-fall deposit observed at distal outcrops. **A:** Location of the distal sites (circles). Sample site locations are shown in the subsequent figures. Base Image (25 April 2015): Nasa Worldview (https://earthdata.nasa.gov/labs/worldview). **B:** The three-layered ash deposit observed at the sites Collón Cura at Argentina. Layers B, C and D are present. **C**: Two-layered deposit of Ruta-40 (Argentina). **D:** Ash fall deposit at Paso Samoré with the layers B, C and D. The thinnest ash deposit is <1 mm and is a unique ash film shown here from Pucón (**E**), Riñinahue (**F**), Ralún (**G**), Concepción (**H**) and Neuquén (**I**).

Fig.3: Stratigraphic correlations of proximal and distal outcrops along two main transects. A-A' shows the sites along the downwind axis, B-B' the crosswind sites.

Fig.4: Plume dispersions of the 22-23 April 2015 eruption. **A:** Eruption plume captured a few minutes after the onset of the eruption on 22 April at 21.38 GMT. **B:** Dispersion of the first plume toward the northeast (~48° azimuth; see arrow) 93 minutes after the start of the eruption. **C:** Start of the second eruption pulse on 23 April at 04.08 GMT. **D:** Detail of the second plume dispersed to the northeast (~55° azimuth; see arrow). **E:** Coexistence of both first and second pulse eruption plumes over southern Chile and Patagonia Argentina on 23 April at 06.35 UTC. **F:** The plume became elongated by 10.08 GMT on 23 April. **G:** The second plume was disconnected from the vent and

dispersed before 13.08 GMT. The scale below the figure shows temperature in °C. The figures **A, B, C, E, F** and **G** are courtesy of the GOES-13 (Goes-East); **D** is from the VIIRS-I-band 5 (NOAA/NASA RAMMB/CIRA).

Fig.5: Isopach maps of deposits. **A** and **B** represent both distal and proximal-medial total deposits. Maps **C, D, E** and **F** show the respective distribution of layers A, B, C and D. Continue lines represent the isopachs in cm, while dotted lines are inferred. Base maps are GDEM shaded relief maps which are a product of Meti and Nasa (http://ava.jpl.nasa.gov/gdem.php?id=1508-02=)

Fig.6: Grain size distribution for proximal (**A**), medial (**B**) and medial-distal (**C**) samples of tephra collected along the dispersal axis. Sample labels can be found in Table 3.

Fig.7: Textures and mineral assemblage of dense and vesiculated pumices revealed by optical microscope. The texture of a dense pumice of layer B revealed by plane- (A) and cross- (B) polarized light. The texture of a vesiculated pumice of layer B revealed by plane- (C) and cross- (D) polarized light. The mineralogical assemblage of pumices consists of plagioclase (plg), orthopyroxene (opx), clinopyroxene (cpx) and Ti-magnetite (ox).

Fig.8: Eruptive model of the 22-23 April eruption deposits and its associated stratigraphic correlation. The drawings are not to scale and their numbers correlate with the description of the eruption dynamics, and with direct observations to the right of the figure.

Fig.9: Tephra volumes of the 22-23 April eruption. **A:** Variability among the three models applied to estimate bulk tephra volumes. **B:** Cumulative volume over time for each model. Note that the hours of eruption do not take into account the pause between the first and second pulse. The curve fitting is exponential. **D:** Thinning trend comparison between layers A, B, C and D. Classification scheme modified from Alfano et al. (2011).

Table captions

Table 1: Synthesis of the Holocene tephra fallouts from Calbuco volcano recognized in the Hualaihue region, according to the work of Watt et al (2011).

Table 2: Sedimentological features of the most representative samples (label). $Mz\Phi_1$, σ_I, Sk_I and K_G are the mean, sorting, skewness and kurtosis, respectively. These parameters were calculated with the Folk and Ward method (1957), using the Gradisat package (Blott and Pye, 2001)

Table 3: Volume calculations for each layer as calculated using different models. *Calculated through the combination of the volumes calculated for the Segments 1 and 2, following the method of Pyle (1989): $T(x) = T_0 e^{-kA^{0.5}}$

**Calculated following the approach of Bonadonna and Houghton (2005). T_{PL} and m are the coefficient and exponent of the power law. Here, we used both proximal (C) and distal (B) limits of integration as C=1 and B=30 for the layers A and D, and C=1 and B=100 for the layers B and C, following the equation: $T(x) = T_{pl} A^{-0.5m}$; $V = \left(\frac{2T_{pl}}{2-m}\right)\left[C^{(2-m)} - B^{(2-m)}\right]$

[1] *Deposit mass = Volume*Density*. We have used a density of 760 kg/m³ (deposit density)

*** Calculated as used in the Weibull function integration (Bonadonna and Costa, 2012). $V = 2\left(\frac{\theta\lambda^2}{n}\right)$. Initial ranges for Θ, λ, n are 0.1-5000 cm, 0.1-1000 km and 0.2-2, respectively.

Table 4: Summary of eruption dynamics as derived from the method of maximum clast diameters (Carey and Sparks, 1986). The density values used here are in Fig. 9.

Downwind and crosswind distances were interpolated and extrapolated from the values given in Table 2 for MLDP and MHDP. Column height (H_t, km acl) has been evaluated with the model and the VER and MDR values were calculated solving the equations of Sparks et al. (1997) for column height: $VER=(H_t/1.67)^{(1/0.251)}$ and $MDR=(H_t/0.220)^{(1/0.251)}$. Finally, the eruption duration (d) is a result of the total erupted mass (TM) or total erupted volume (TV), divided by the respective VER or MDR: d=TV/VER; d=TM/MDR. Note that TM and TV are average values obtained from Table 3. The bold-type values are considered as the most realistic when compared with the direct and satellite observations of the eruption evolution.

Table 5: Magnitude and Intensity from Pyle (2000) associated with the tephra fall deposits of the 22-23 April eruption at Calbuco volcano. Magnitude is defined as $M=\log_{10}(TM)-7$ and Intensity is $I=\log_{10}(MDR)+3$. The values of TM and MDR are derived from Table 4.

TABLES

Table 1:

Tephra Unit	Age yr BP	Type	SiO2 %	Dispersal Axis	Volume [km3]	Mass $x10^{12}$	Magnitude
Ca13	1304-1180	Pumice-fall	57	SE	0.5	0.4	>4.5
Ca12	1919-1654	Pumice-fall		ESE	0.8	0.7	≤5
Ca11	7162-6800	Pumice-fall		SE	0.9	0.7	~5
Ca10	8652-6892	Pumice-fall		SE	0.4	0.3	>4.5
Ca9	9285-7214	Ash-fall					
Ca8	9529-7881	Scoria-fall?		E	1.1	0.9	>5
Ca7	9745-9452	Pumice-fall	65	ESE	0.4	0.4	>4.5
Ca6	10157-9505	Pumice-fall					
Ca5	10222-9643	Pumice-fall					
Ca4	10345-9745	Pumice-fall					
Ca3	10445-9870	Pumice-fall					
Ca2	10526-10023	Pumice-fall					
Ca1	10571-10254	Pumice-fall	50	SE	1.2	1	>5

Table 2:

Label	Layer	Thickness [cm]	Largest clast [cm] MLDP [cm]	MHDP [cm]	Lithic [cm]	Abundance [%] LDP	HDP	Lithic	Grainsize $Mz_{\Phi I}$	σ_I	Sk_I	K_G	Distance [km]
DF-02	A	4	2.9	2.9	1.3	~90	~10	~0.2					7
DF-02	B	7											7
DF-02	C	5	6.8	2.8	2	~70	~30	~0.2					7
DF-02	D	2	3.8	4.8	2.8	~30	~70	~0.2					7
DF-05	A	2	1	1.3		~80	~20	~0.2	-1.414	1.124	-0.177	0.949	15
DF-05	BC	3											15
DF-05		6	2.4	1.2		~80	~20	~0.2	-1.424	1.199	-0.209	0.907	15
DF-05	D	2							-0.880	0.854	-0.252	1.008	15
DF-10	A	10	3.5	2.5	2	~90	~10	~0.2	-3.079	1.068	0.125	0.899	5
DF-10	B	14							-3.662	1.478	0.458	0.860	5
DF-10	C	25	7.2	4.1	2.5	~90	~10	~0.2	-2.514	1.201	0.075	0.958	5
DF-10	D	8	2.9	3.3	1.7	~10	~90	~0.2	-2.844	1.454	0.359	1.841	5
KAL-18	AB	8.5	1						-0.543	0.790	-0.078	0.926	16
KAL-18	CD	9.7	0.6		0.4				-0.864	0.824	0.243	0.819	16
KAL-21	AB	13	1.5						-0.518	0.788	-0.076	0.972	15
KAL-21	CD	3	0.8		0.7				-0.591	0.791	-0.074	0.852	15
DF-08	BC	1							0.813	0.630	-0.040	0.906	27
DF-08	D	5							0.939	0.490	0.035	0.994	27

Table 3:

	PROXIMAL-MEDIAL REGIME					PROXIMAL-DISTAL
UNIT	**A**	**B**	**C**	**D**	**Whole deposit (A+B+C+D)**	**Whole deposit (A+B+C+D)**
Erupted Volume (km³)						
Exponential thinning *	8.61E-03	3.40E-02	5.03E-02	1.24E-02	**1.05E-01**	**2.70E-01**
number of isopachs	4	5	5	4	5	10
mean rel. squared error		1.07E-01	9.44E-02	5.30E-31	6.72E-02	0.085
Segment 1	5.24E-03	1.53E-02	1.30E-02	2.39E-03		6.74E-02
c	0.23	0.22	0.31	2.42		0.8577
m	0.25	0.14	0.07	1.37		0.1524
Segment 2	3.37E-03	1.87E-02	3.74E-02	9.96E-03		2.03E-01
c	0.1223	0.06	0.169	0.04691		0.02136
m	0.1829	0.07	0.0877	0.09531		0.01411
Power Law **	1.12E-02	3.32E-02	6.43E-02	1.00E-02	**1.19E-01**	**2.77E-01**
number of isopachs	4	5	5	4	5	10
mean rel. squared error	3.17E-02	4.42E-02	5.41E-02	2.23E-02	3.81E-02	8.08E-02
PL-coefficient(T_{PL})	0.66	0.82	1.08	0.16		7.65
PL-Exponent (m)	1.529	1.31	1.17	0.99		1.70
Proximal Limit	1	1	1	1		1
Distal Limit	30	50	50	30		450
Weibull method ***	2.16E-02	3.09E-02	5.09E-02	3.71E-02	**1.40E-01**	**2.67E-01**
number of isopachs	4	5	5	4	5	10
mean rel. squared error	3.07E-03	3.84E-02	3.14E-02	1.98E-02	2.32E-02	0.10
Θ	0.04781	0.02025	0.05634	0.0002		0.01
λ	38.80	25.85	23.44	974.2		99.97
n	0.67	0.94	1.22	1.04		0.90
Erupted Mass (kg)						
Exponential derived	6.32E+09	2.50E+10	2.69E+10	6.61E+09	**1.05E+11**	**2.69E+11**
Power Law derived	8.20E+09	2.44E+10	3.44E+10	5.35E+09	**1.18E+11**	**2.76E+11**
Weibull derived	1.58E+10	2.20E+10	2.64E+10	2.09E+10	**1.40E+11**	**2.66E+11**

Table 4:

Unit	Density (kg/m3)	Diameter [cm]	Downwind [km]	Crosswind [km]	H_t [km] acl	VER [m^3/s]	MDR [kg s^{-1}]	Duration [h]
A	760	2.62	9.01	3.33	9.3	7.58E+02	1.90E+06	1.48
A	**1670**	**2.4**	**8.15**	**2.37**	**12.09**	**2.09E+03**	**5.23E+06**	**0.54**
A	2190	2.4	4.75	1.76	10.23	1.09E+03	2.74E+06	1.03
B-C	760	5.26	8.78	3.2	14.5	4.21E+03	1.05E+07	5.86
B-C	**1670**	**2.4**	**10.31**	**3.52**	**15.38**	**5.28E+03**	**1.32E+07**	**4.67**
B-C	2190	1.83	9.3	3.2	14.5	4.21E+03	1.05E+07	5.86
D	760	2.62	9.5	3.15	9.05	6.82E+02	1.71E+06	7.64
D	1670	4.84	6.36	1.7	11.78	1.89E+03	4.73E+06	2.76
D	**2190**	**1.83**	**8.05**	**2.74**	**13.18**	**2.91E+03**	**7.29E+06**	**1.79**

Table 5:

Mass of the total (proximal-distal) [kg]	A (22 April)	B (22 April)	C (23 April)	D (23 April)	Whole deposit (A+B+C+D)
Average	1.01E+10	8.31E+10	1.39E+11	4.70E+10	2.80E+11
Duration [s]	684	4.72E+03	6.36E+03	1.53E+04	27096
MDR [kg/s]	1.48E+07	1.76E+07	2.19E+07	3.06E+06	1.03E+07
Magnitude	3.01	3.92	4.14	3.67	4.45
Intensity	10.17	10.25	10.34	9.49	10.01

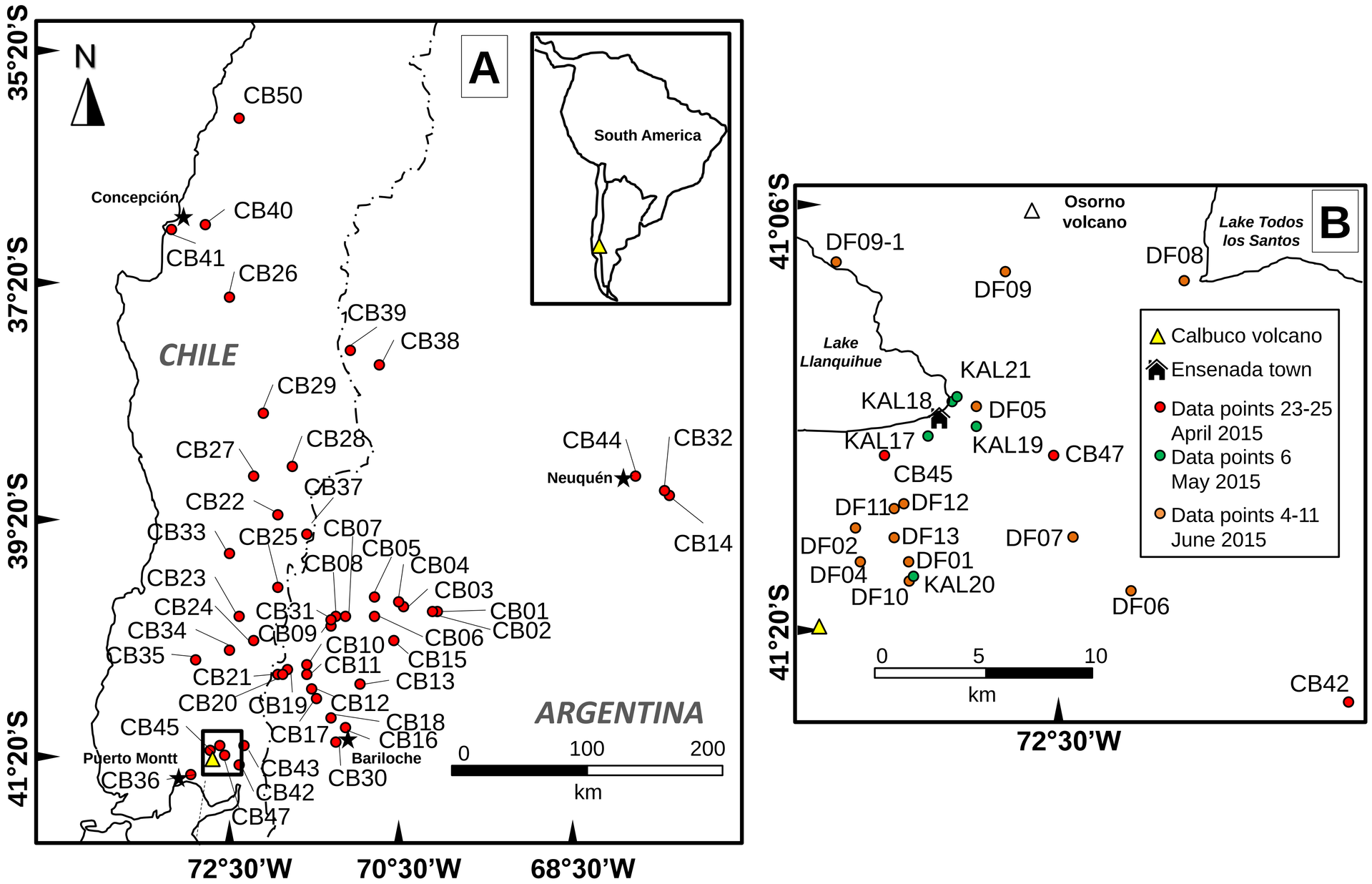
A
N
35°20'S
37°20'S
39°20'S
41°20'S
72°30'W
70°30'W
68°30'W
CHILE
ARGENTINA
Concepción
Neuquén
Bariloche
Puerto Montt
South America
CB50
CB40
CB41
CB26
CB39
CB38
CB29
CB27
CB28
CB37
CB22
CB33
CB25
CB07
CB05
CB08
CB04
CB23
CB03
CB24
CB31
CB01
CB34
CB09
CB06
CB02
CB35
CB10
CB15
CB11
CB21
CB13
CB20
CB19
CB12
CB45
CB18
CB17
CB16
CB43
CB30
CB36
CB42
CB47
CB44
CB32
CB14
0
100
200
km
B
41°06'S
41°20'S
72°30'W
Osorno volcano
Lake Todos los Santos
Lake Llanquihue
DF09-1
DF09
DF08
KAL21
KAL18
DF05
KAL17
KAL19
CB47
CB45
DF11
DF12
DF02
DF13
DF07
DF01
DF04
KAL20
DF10
DF06
CB42
Calbuco volcano
Ensenada town
Data points 23-25 April 2015
Data points 6 May 2015
Data points 4-11 June 2015
0
5
10
km

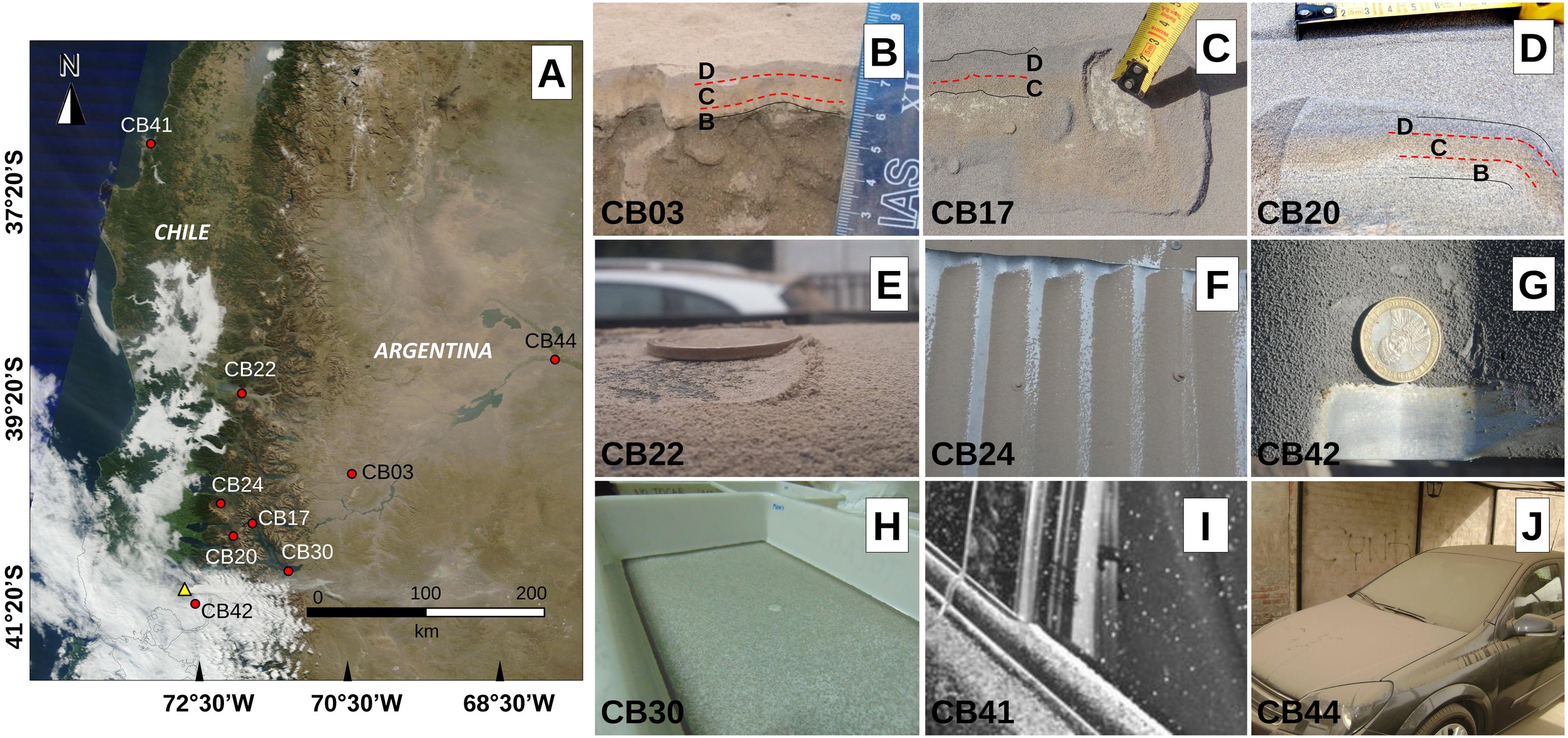
A
N
CB41
CHILE
ARGENTINA
CB44
CB22
CB03
CB24
CB17
CB20
CB30
CB42
0
100
200
km
37°20'S
39°20'S
41°20'S
72°30'W
70°30'W
68°30'W
B
D
C
B
CB03
C
D
C
CB17
D
D
C
B
CB20
E
CB22
F
CB24
G
CB42
H
CB30
I
CB41
J
CB44

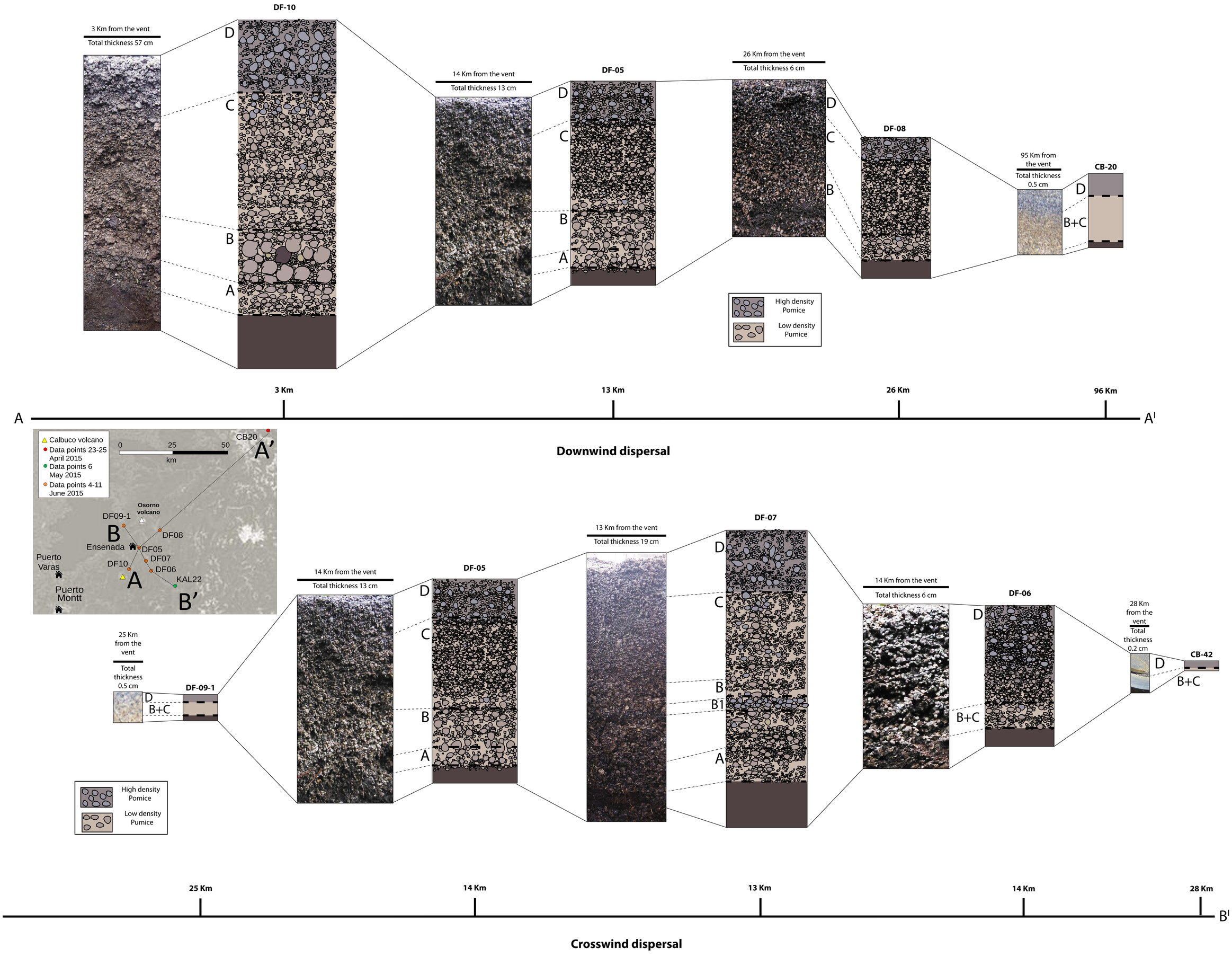
3 Km from the vent
Total thickness 57 cm
DF-10
D
C
B
A
14 Km from the vent
Total thickness 13 cm
DF-05
D
C
B
A
26 Km from the vent
Total thickness 6 cm
DF-08
D
C
B
95 Km from the vent
Total thickness 0.5 cm
CB-20
D
B+C
High density Pomice
Low density Pumice
3 Km
13 Km
26 Km
96 Km
A
A'
Calbuco volcano
Data points 23-25 April 2015
Data points 6 May 2015
Data points 4-11 June 2015
0
25
50
km
CB20
A'
Osorno volcano
DF09-1
B
DF08
Ensenada
DF05
DF07
DF06
DF10
A
KAL22
Puerto Varas
Puerto Montt
B'
Downwind dispersal
25 Km from the vent
Total thickness 0.5 cm
DF-09-1
D
B+C
14 Km from the vent
Total thickness 13 cm
DF-05
D
C
B
A
13 Km from the vent
Total thickness 19 cm
DF-07
D
C
B
B1
A
14 Km from the vent
Total thickness 6 cm
DF-06
D
B+C
28 Km from the vent
Total thickness 0.2 cm
CB-42
D
B+C
High density Pomice
Low density Pumice
25 Km
14 Km
13 Km
14 Km
28 Km
B
B'
Crosswind dispersal

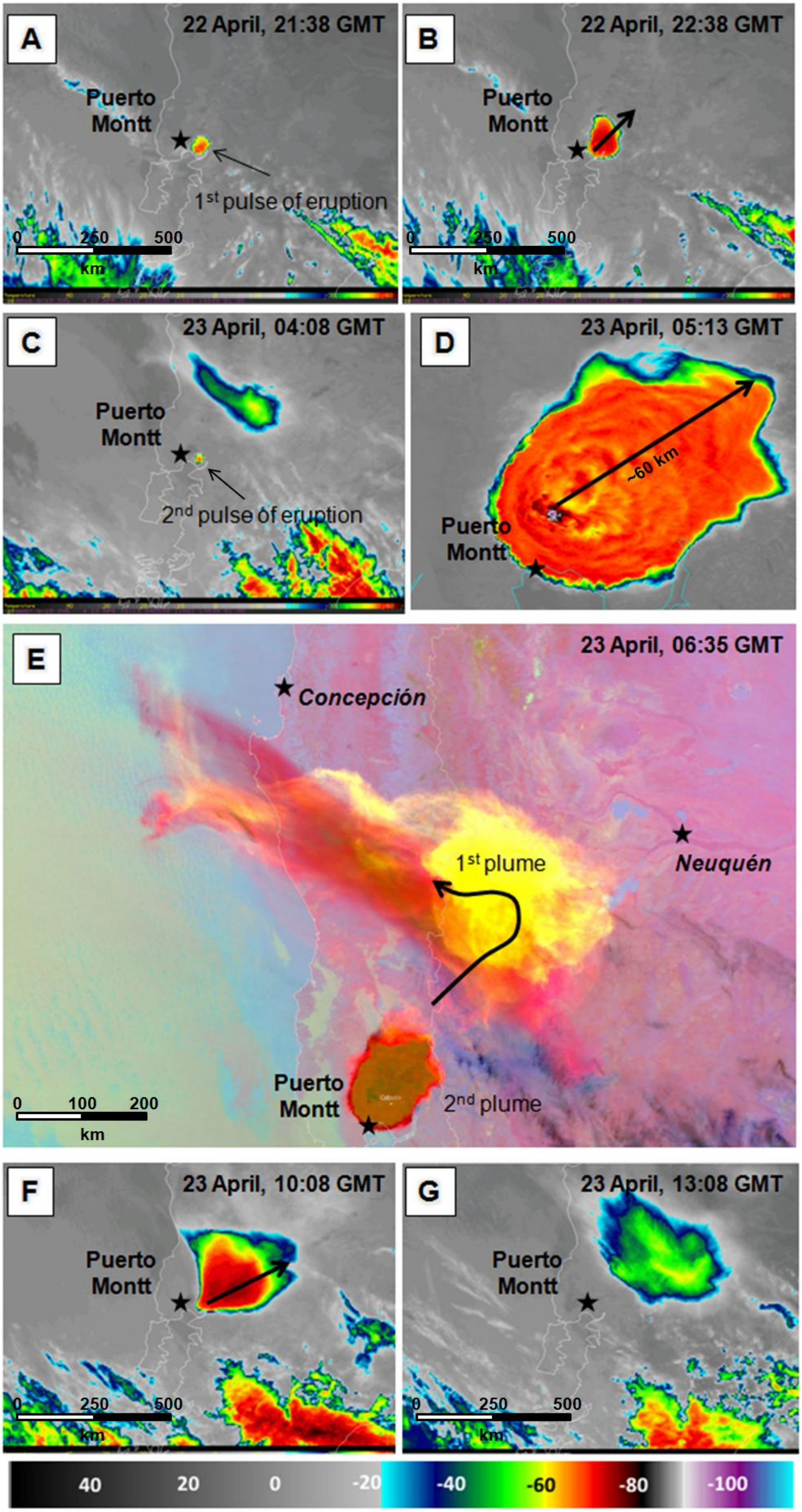
A
22 April, 21:38 GMT
Puerto Montt
1st pulse of eruption
0 250 500
km
B
22 April, 22:38 GMT
Puerto Montt
0 250 500
km
C
23 April, 04:08 GMT
Puerto Montt
2nd pulse of eruption
D
23 April, 05:13 GMT
~60 km
Puerto Montt
E
23 April, 06:35 GMT
Concepción
Neuquén
1st plume
Puerto Montt
2nd plume
0 100 200
km
F
23 April, 10:08 GMT
Puerto Montt
0 250 500
km
G
23 April, 13:08 GMT
Puerto Montt
0 250 500
km
40 20 0 -20 -40 -60 -80 -100

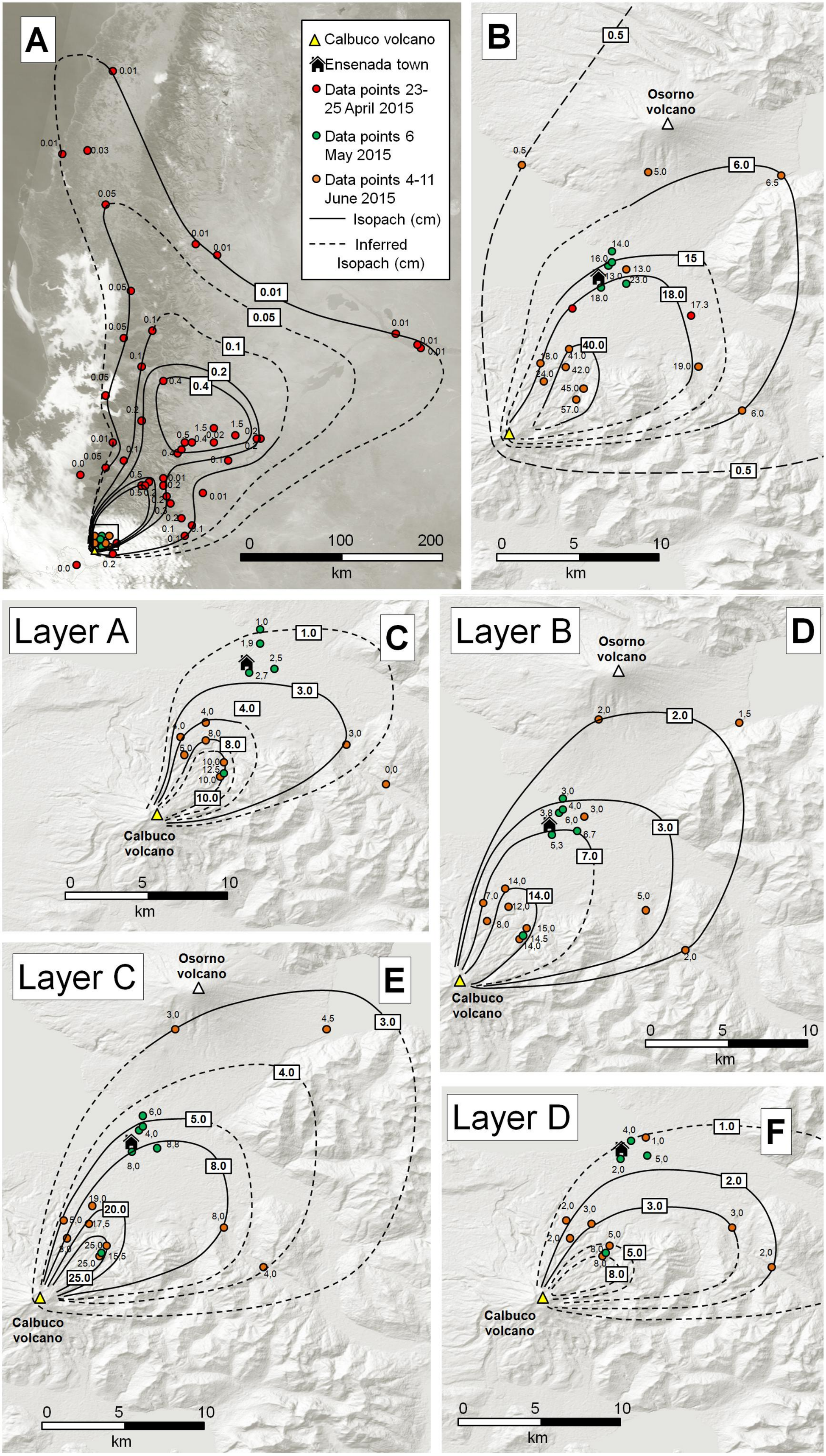
A
Calbuco volcano
Ensenada town
Data points 23-25 April 2015
Data points 6 May 2015
Data points 4-11 June 2015
Isopach (cm)
Inferred Isopach (cm)
0.01
0.05
0.1
0.2
0.4
0 100 200
km
B
Osorno volcano
0.5
6.0
15
18.0
40.0
0 5 10
km
Layer A
C
1.0
3.0
4.0
8.0
10.0
Calbuco volcano
0 5 10
km
Layer B
D
Osorno volcano
2.0
3.0
7.0
14.0
Calbuco volcano
0 5 10
km
Layer C
E
Osorno volcano
3.0
4.0
5.0
8.0
20.0
25.0
Calbuco volcano
0 5 10
km
Layer D
F
1.0
2.0
3.0
5.0
8.0
Calbuco volcano
0 5 10
km

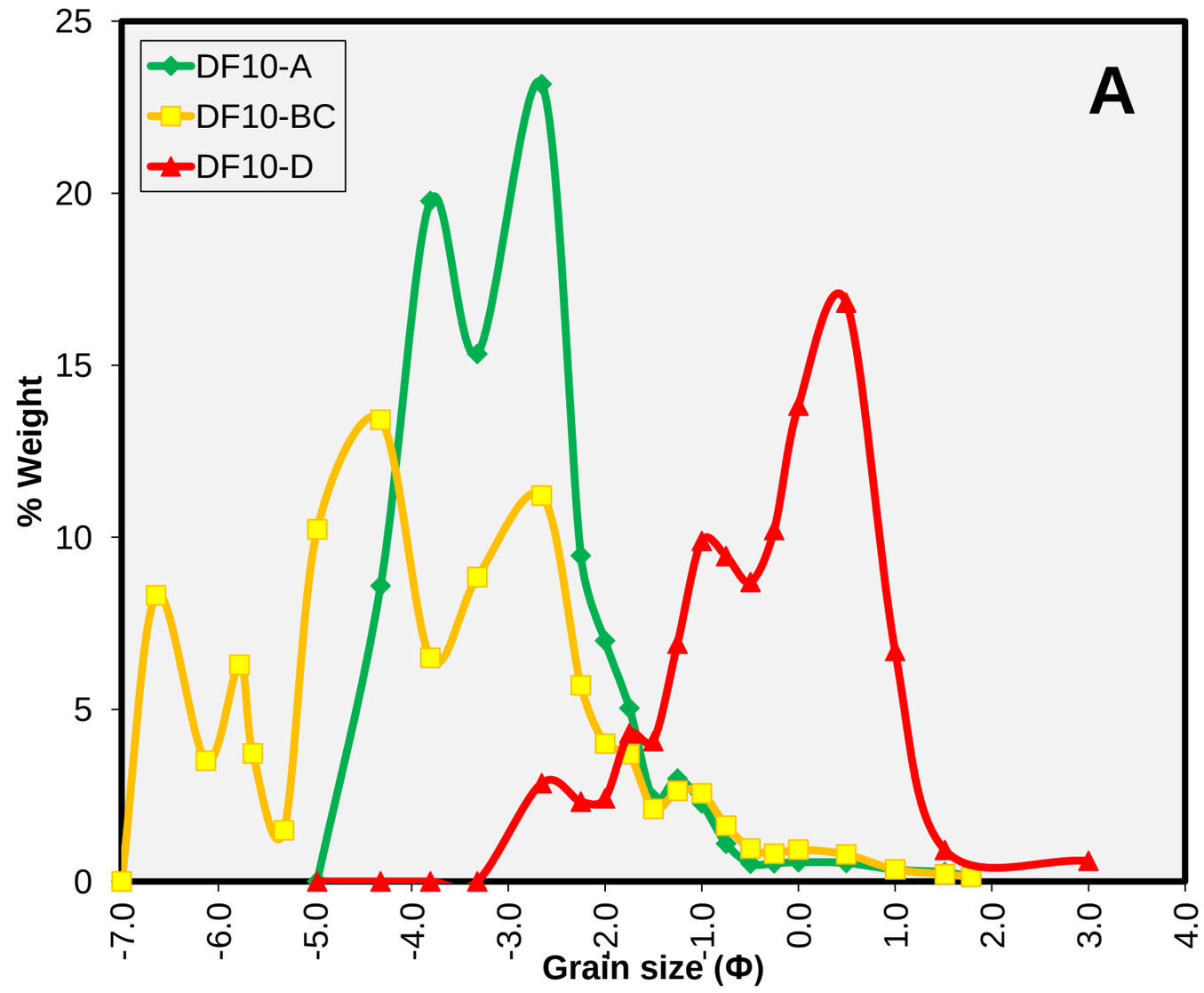
A
DF10-A
DF10-BC
DF10-D
% Weight
Grain size (Φ)
25
20
15
10
5
0
-7.0
-6.0
-5.0
-4.0
-3.0
-2.0
-1.0
0.0
1.0
2.0
3.0
4.0

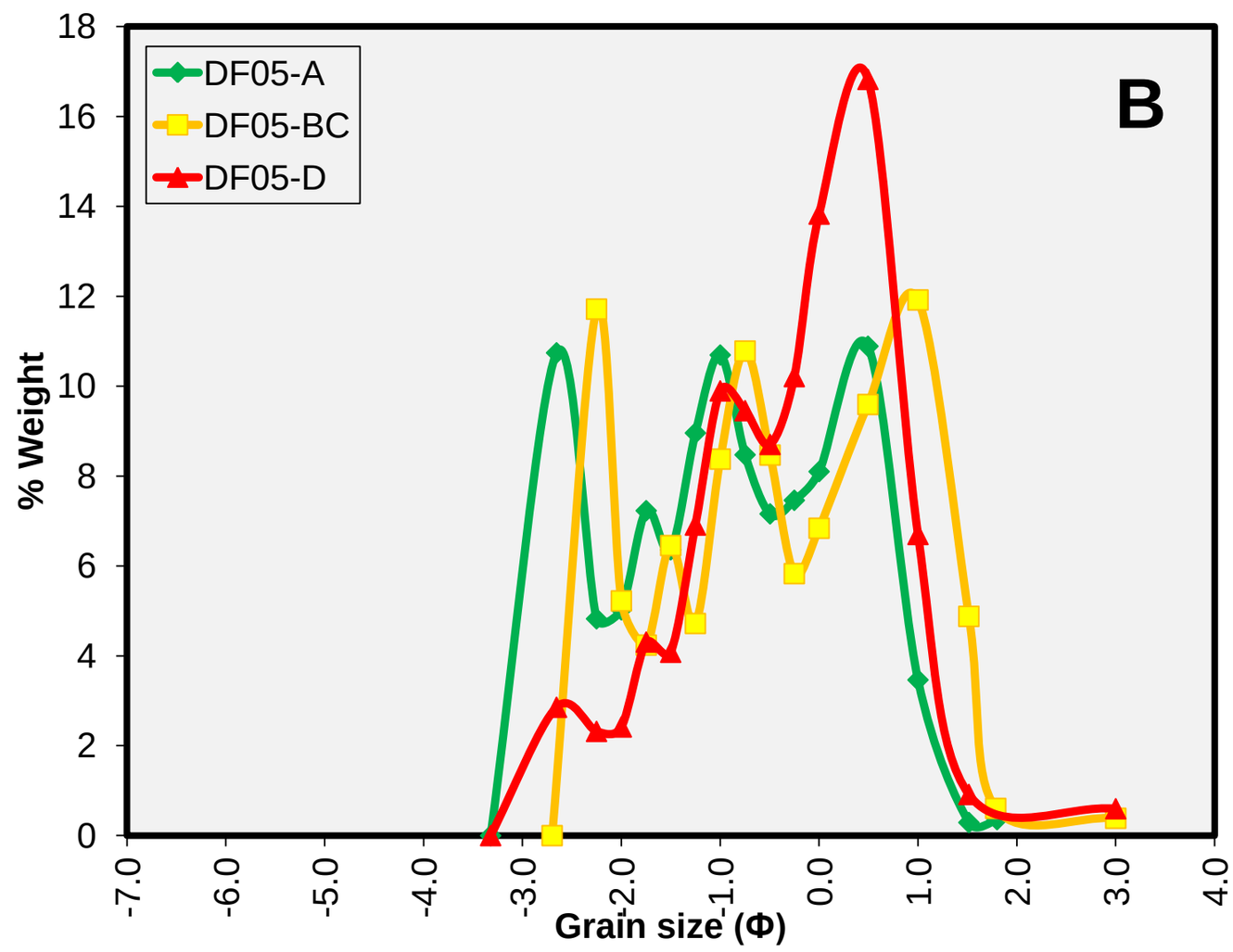
B
DF05-A
DF05-BC
DF05-D
% Weight
Grain size (Φ)
18
16
14
12
10
8
6
4
2
0
-7.0
-6.0
-5.0
-4.0
-3.0
-2.0
-1.0
0.0
1.0
2.0
3.0
4.0

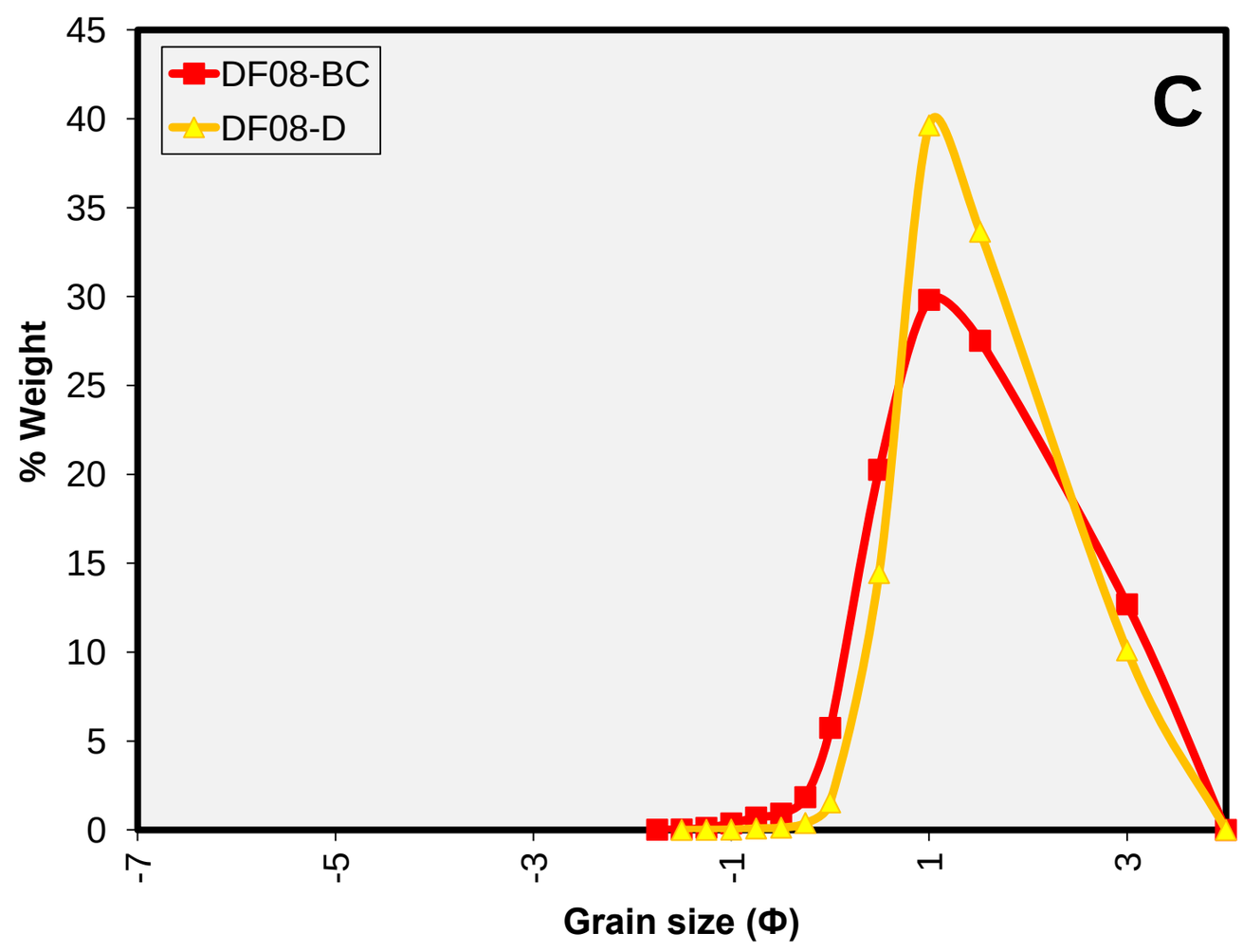
C
DF08-BC
DF08-D
% Weight
Grain size (Φ)
45
40
35
30
25
20
15
10
5
0
-7
-5
-3
-1
1
3

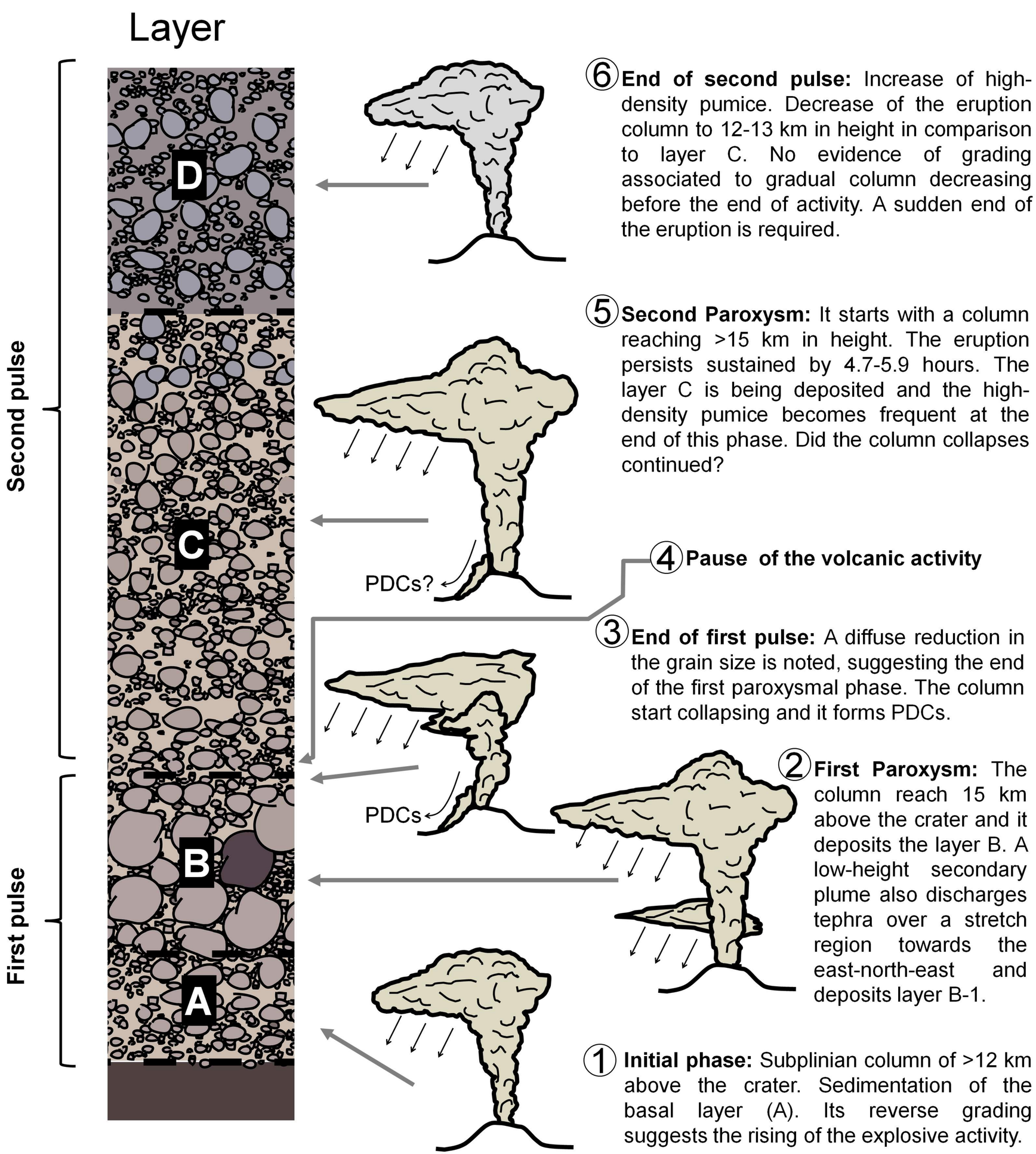

⑥ **End of second pulse:** Increase of high-density pumice. Decrease of the eruption column to 12-13 km in height in comparison to layer C. No evidence of grading associated to gradual column decreasing before the end of activity. A sudden end of the eruption is required.

⑤ **Second Paroxysm:** It starts with a column reaching >15 km in height. The eruption persists sustained by 4.7-5.9 hours. The layer C is being deposited and the high-density pumice becomes frequent at the end of this phase. Did the column collapses continued?

④ **Pause of the volcanic activity**

③ **End of first pulse:** A diffuse reduction in the grain size is noted, suggesting the end of the first paroxysmal phase. The column start collapsing and it forms PDCs.

② **First Paroxysm:** The column reach 15 km above the crater and it deposits the layer B. A low-height secondary plume also discharges tephra over a stretch region towards the east-north-east and deposits layer B-1.

① **Initial phase:** Subplinian column of >12 km above the crater. Sedimentation of the basal layer (A). Its reverse grading suggests the rising of the explosive activity.

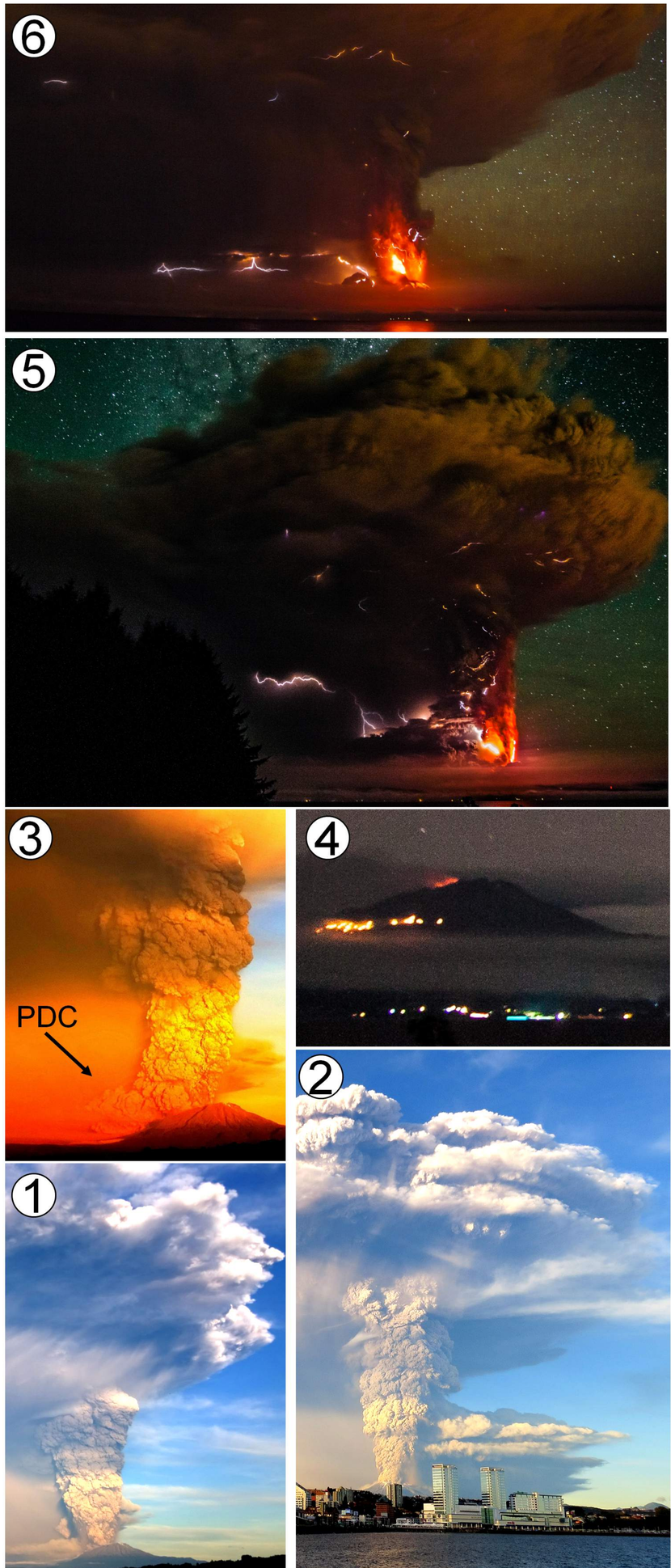

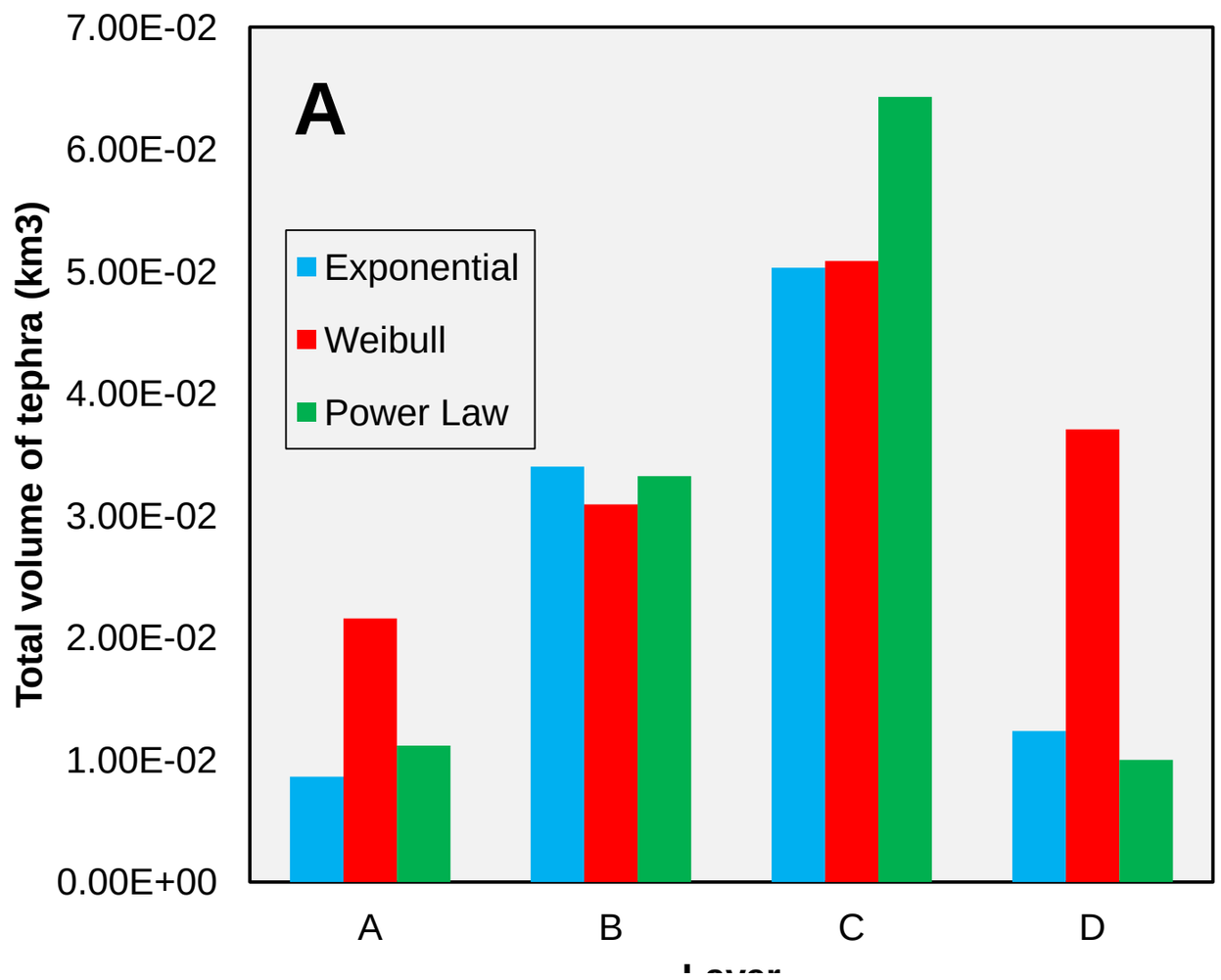
A
Exponential
Weibull
Power Law
Total volume of tephra (km3)
7.00E-02
6.00E-02
5.00E-02
4.00E-02
3.00E-02
2.00E-02
1.00E-02
0.00E+00
A
B
C
D

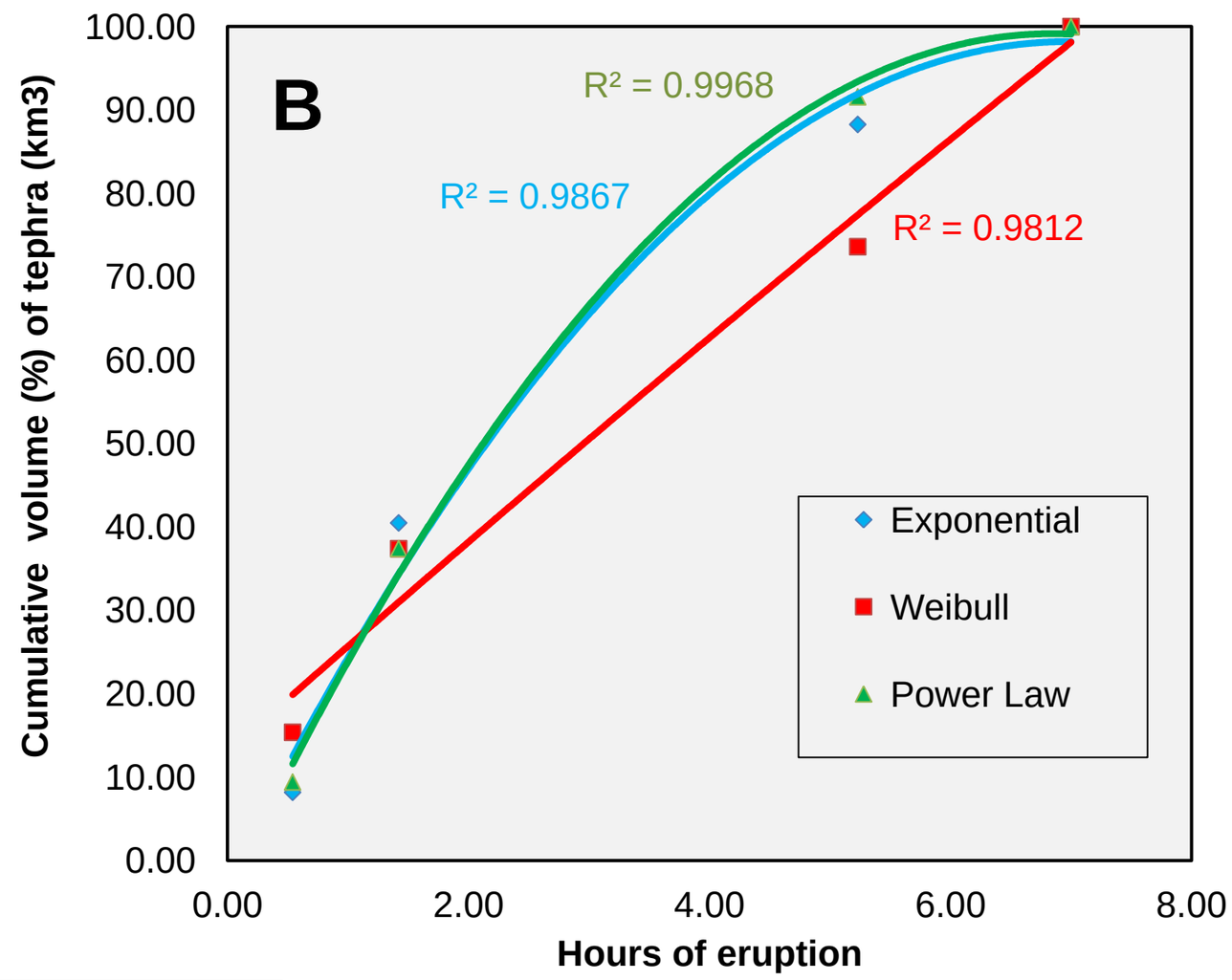
B
R² = 0.9968
R² = 0.9867
R² = 0.9812
Exponential
Weibull
Power Law
Cumulative volume (%) of tephra (km3)
100.00
90.00
80.00
70.00
60.00
50.00
40.00
30.00
20.00
10.00
0.00
0.00
2.00
4.00
6.00
8.00
Hours of eruption

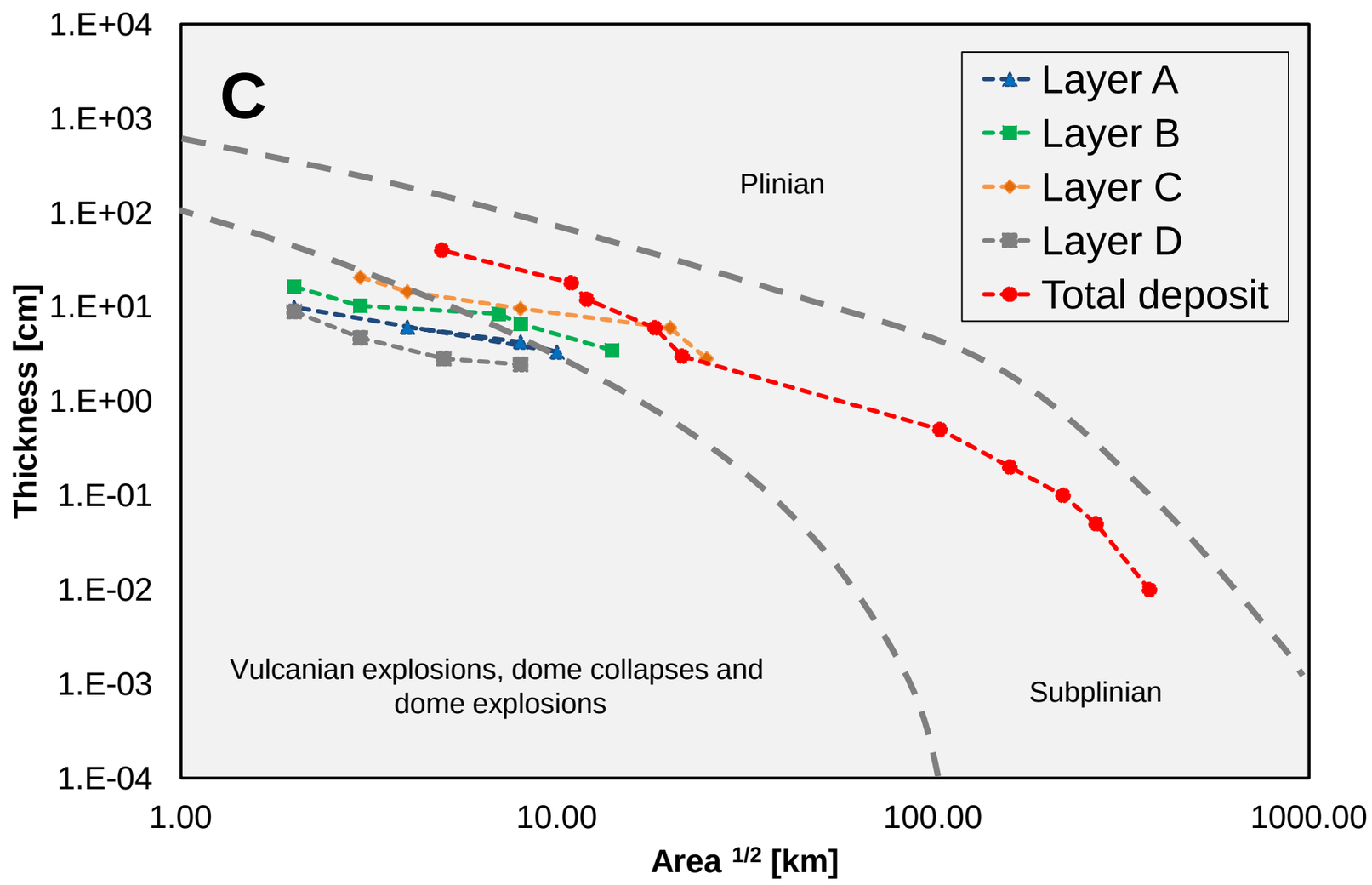
C
Layer A
Layer B
Layer C
Layer D
Total deposit
Plinian
Vulcanian explosions, dome collapses and dome explosions
Subplinian
Thickness [cm]
1.E+04
1.E+03
1.E+02
1.E+01
1.E+00
1.E-01
1.E-02
1.E-03
1.E-04
1.00
10.00
100.00
1000.00
Area 1/2 [km]